Impact of tide-topography interactions on basal melting of Larsen C Ice Shelf, Antarctica

R. D. Mueller,[1,2] L. Padman,[2] M. S. Dinniman,[3] S. Y. Erofeeva,[1] H. A. Fricker,[4] and M. A. King[5]

[1]   Basal melting of ice shelves around Antarctica contributes to formation of Antarctic Bottom Water and can affect global sea level by altering the offshore flow of grounded ice streams and glaciers. Tides influence ice shelf basal melt rate (w_b) by contributing to ocean mixing and mean circulation as well as thermohaline exchanges with the ice shelf. We use a three-dimensional ocean model, thermodynamically coupled to a nonevolving ice shelf, to investigate the relationship between topography, tides, and w_b for Larsen C Ice Shelf (LCIS) in the northwestern Weddell Sea, Antarctica. Using our best estimates of ice shelf thickness and seabed topography, we find that the largest modeled LCIS melt rates occur in the northeast, where our model predicts strong diurnal tidal currents ($\sim$0.4 m s^{-1}). This distribution is significantly different from models with no tidal forcing, which predict largest melt rates along the deep grounding lines. We compare several model runs to explore melt rate sensitivity to geometry, initial ocean potential temperature (θ_0), thermodynamic parameterizations of heat and freshwater ice-ocean exchange, and tidal forcing. The resulting range of LCIS-averaged w_b is $\sim$0.11–0.44 m a^{-1}. The spatial distribution of w_b is very sensitive to model geometry and thermodynamic parameterization while the overall magnitude of w_b is influenced by θ_0. These sensitivities in w_b predictions reinforce a need for high-resolution maps of ice draft and sub-ice-shelf seabed topography together with ocean temperature measurements at the ice shelf front to improve representation of ice shelves in coupled climate system models.

1.   Introduction

[2]   The oceans around Antarctica interact with the continental ice sheet at the floating ice shelves that occupy about 50% of its coastline [*Drewry et al.*, 1982]. Melting at an ice shelf base influences global ocean properties by producing cold and low-salinity meltwater plumes that carry freshwater mass away from the continent and precondition the surrounding continental shelf waters for formation of Antarctic Bottom Water [e.g., *Jacobs*, 2004]. Basal melting can also weaken an ice shelf, increasing the likelihood of calving events or disintegration [*Vieli et al.*, 2007]. The balance between ice gain (by advective input of grounded ice, snow accumulation, and marine ice accretion) and loss (primarily basal melting and calving) determines the total mass balance of an ice shelf. Ice shelf stability can be compromised when the mass balance is negative. Mass loss reduces the stresses impeding the offshore flow of the ice shelves and leads to more rapid seaward ice transport in the inflowing glaciers and ice streams [*Rignot et al.*, 2004; *Scambos et al.*, 2004]. Through these processes, the ocean can affect the overall mass balance of the Antarctic ice sheet and associated global sea level on decadal time scales [*Payne et al.*, 2004].

[3]   While we have a general understanding of processes that cause ice shelf basal melting [*Lewis and Perkin*, 1986; *MacAyeal*, 1984; *Hellmer and Olbers*, 1989; *Jacobs et al.*, 1992; *Holland and Jenkins*, 1999], the ability to accurately model the spatial distribution of basal melt rate (w_b) and the associated net ice mass loss is limited by several factors, including: poorly known ice shelf and seabed geometry, a paucity of hydrographic data defining the nature of the ocean inflow to the sub-ice-shelf cavity, and neglect of specific processes for the purpose of computational ease and efficiency. Models that attempt to project land ice contribution

[1]College of Earth, Ocean, and Atmospheric Sciences, Oregon State University, Corvallis, Oregon, USA.
[2]Earth & Space Research, Corvallis, Oregon, USA.
[3]Center for Coastal Physical Oceanography, Old Dominion University, Norfolk, Virginia, USA.
[4]Institute of Geophysics and Planetary Physics, Scripps Institution of Oceanography, University of California, San Diego, La Jolla, California, USA.
[5]School of Civil Engineering and Geosciences, Newcastle University, Newcastle upon Tyne, UK.

to sea level changes over long time scales [e.g., *Pollard and DeConto*, 2009] will be subject to potentially large errors until these data and model deficiencies are resolved.

[4] One forcing that is usually excluded in numerical models of ice shelf basal melting is tides. A relationship between tides and basal melting was postulated by *MacAyeal* [1984], who noted that the ice shelf isolates the sub-ice-shelf cavity from direct wind forcing and, hence, increases the importance of tidal currents as a source of oceanic kinetic energy for conversion to mixing. More recent studies have demonstrated that tides can be a significant factor in ocean and ice shelf interactions close to the ice shelf boundaries [*Makinson and Nicholls*, 1999; *Makinson*, 2002; *Joughin and Padman*, 2003; *Holland*, 2008; *Robinson et al.*, 2010]. *Makinson et al.* [2011] predicted that tides contribute approximately half of the net mass loss from Filchner-Ronne Ice Shelf (FRIS) in the southern Weddell Sea.

[5] In this paper, we are interested in understanding basal melt sensitivity to errors in initial and boundary conditions for ice shelves where tidal forcing is significant. For this purpose, we report on sensitivity studies of the effects of adding tides to an ocean model that is thermodynamically coupled to Larsen C Ice Shelf (LCIS) in the northwestern Weddell Sea, Antarctica. This ice shelf experiences significant tidal variability [*King et al.*, 2011] and is ventilated by cold, High Salinity Shelf Water (HSSW) [*Nicholls et al.*, 2004]; it is similar, therefore, in some respects to the much larger FRIS studied by *Makinson et al.* [2011]. The smaller size of LCIS is advantageous for studying the influence of tides in these conditions because it allows for much finer model grid resolution. The more northerly location of LCIS also means that it will likely respond to climate change earlier than FRIS. Recent lowering of the LCIS surface [*Shepherd et al.*, 2003; *Fricker and Padman*, 2012] supports the view that LCIS is undergoing changes that may lead to weakening of the ice shelf.

[6] Atmospheric forcing and open ocean circulation clearly play important roles in ice shelf mass and elevation variability [*Fricker and Padman*, 2012], but in the present study we only force our models with tides. Our approach allows us to focus on understanding the factors contributing to uncertainty in w_b. For LCIS, relevant sources of uncertainties include water column thickness (*wct*), temperature of ocean water flowing into the sub-ice-shelf cavity, and the parameterization of heat and freshwater exchange at the ice-ocean interface. We are particularly interested in the effect of errors in *wct*. Tidal currents can be very sensitive to *wct* errors on small spatial scales, leading to significant uncertainty in the contribution of tides to w_b. This study complements the application of a plume model to LCIS [*Holland et al.*, 2009], which provides a valuable comparison for our simulations.

[7] We first explain the fundamentals of ice and ocean interaction in section 2. Readers who are already familiar with ice-ocean interaction may proceed directly to sections 2.1 and 2.2, which offer background information specific to tides and LCIS, respectively. We then discuss model configuration (section 3) and results from the set of simulations that we use to explore model sensitivity (section 4). The conclusions (section 5) first describe how these results apply to LCIS and then generalize them to all ice shelves. Auxiliary material is provided to explain the methodology used to create the model geometry and the details of our numerical setup.[1] Auxiliary material also includes information on ice draft, bathymetry, and our evaluation of model grid errors.

2. Background

[8] A simplified characterization of sub-ice-shelf cavity circulation is the "ice pump" concept [*Lewis and Perkin*, 1986], in which the increased pressure in the grounding zone (i.e., the region near the grounding line) suppresses the in situ freezing point (T_f) of seawater, increasing the difference between ocean temperature (T_o) and T_f. This increased thermal difference fuels the melting of the meteoric ice in the grounding zone and introduces a buoyant plume of cold, fresh water that entrains ambient water as it ascends through the water column along the sloping ice shelf base. The loss of pressure as the plume rises may result in ice accretion onto the ice shelf base, thus, "pumping" ice away from the grounding zone and possibly redistributing it downstream. Alternatively, if the plume reaches the depth of neutral buoyancy, it can separate from the ice shelf base and/or be exported from the ice shelf cavity. By the time this plume leaves the ice shelf cavity it is estimated to contain a melt-water concentration of ~0.2–2%, depending on the magnitude of w_b and the corresponding strength of the plume [*Mackensen*, 2001; *Payne et al.*, 2007]. Back at the grounding zone, the ascending plume is replaced by relatively unmodified, hence warmer, ocean water to maintain the thermohaline circulation.

[9] This theoretical ice pump is often used to describe ice shelf basal melting; however, it focuses on the influence of pressure on thermal forcing, which emphasizes melting of the deep ice along the grounding zone. In reality, melting can occur at a variety of locations from the grounding zone to the ice shelf front [e.g., *Joughin and Padman*, 2003]. Buoyant meltwater plumes can extend far from their initial sources, and the characteristics of a plume will depend not only on local properties such as ice base topography and turbulent kinetic energy but also the accumulated history of the plume. The complexity of coupling local turbulent and thermodynamic processes with advection prevents an exact characterization of specific plumes.

[10] Melting in the grounding zone is important because it tends to increase the along-flow ice surface slope and the net force driving ice offshore [*Joughin et al.*, 2010; *Little et al.*, 2012] with a direct impact on ice sheet mass balance [*Rignot and Jacobs*, 2002]. Meltwater from this region is also the coldest. In addition, the grounding zone is where *wct* goes to zero and where fresh subglacial water first enters the ocean after draining from under the grounded ice. Plumes from this meltwater will reflect the details of ice base topography [*Little et al.*, 2009], tides [*Holland*, 2008], the temperature of the ambient ocean, and the depression of salinity due to inflow from subglacial freshwater. The latter dependence has been shown to be critical to basal melting near the grounding line of tidewater glaciers and ice shelves [*Motyka et al.*, 2003, 2011; *Rignot et al.*, 2010; *Jenkins*, 2011].

---

[11] As ice draft becomes shallower, away from the grounding line, melting requires a greater supply of ocean heat to compensate for the smaller pressure suppression of T_f and generally weaker ice base slopes. In some regions (e.g., the Amundsen Sea), the principal water mass ventilating the sub-ice-shelf cavities is Circumpolar Deep Water (CDW) whose temperature (often > 1°C) is already much greater than T_f; therefore, we expect that variations in CDW inflow depth and temperature have a greater influence on w_b than the pressure effect on T_f. For an ice shelf in this region, such as the floating portion of Pine Island Glacier, the associated melt can exceed 100 m a^{-1} [*Payne et al.*, 2007; *Joughin et al.*, 2010; *Bindschadler et al.*, 2011]. Basal melt may also be augmented near the ice shelf front during the summer months when the upper ocean water masses adjacent to the front become warmer and are episodically advected into the ice shelf cavity by wind forcing and tides [e.g., *Horgan et al.*, 2011].

2.1. Tides

[12] Tidal height variability beneath Antarctic ice shelves is relatively easy to monitor with in situ measurements [e.g., *King et al.*, 2011] and with satellite radar and laser altimetry [e.g., *Fricker and Padman*, 2002; *Padman et al.*, 2008] because the ice shelf is floating and responds immediately to surface elevation changes of the ocean. However, tidal currents under ice shelves, which are thermodynamically more relevant, are more challenging to measure. Only a few ocean current time series are available from moorings deployed through boreholes drilled in George VI Ice Shelf [*Potter and Paren*, 1985], FRIS [*Nicholls et al.*, 1997] and Amery Ice Shelf [*Craven et al.*, 2009]. As a result, most of our understanding of tidal currents under and near ice shelves has been obtained from models.

[13] The documented effects of tides on ice shelf basal melting are complex. Tides may intensify the entrainment of warmer water beneath the cooler boundary layer to increase w_b [*MacAyeal*, 1984], but they can also create a well-mixed region that diminishes w_b in the grounding zone, landward of a tidal front [*Holland*, 2008]. Through their interactions with topography and nontidal flows, tides can contribute to the mean circulation into and within an ice shelf cavity [*Makinson and Nicholls*, 1999]. Other studies confirm the importance of tides for ice-ocean interactions on FRIS [*Makinson*, 2002] and Ross Ice Shelf [*MacAyeal*, 1985b; *Robinson et al.*, 2010]. It is likely that the relatively high basal melt rates found near the Ross Ice Shelf calving front are influenced by tidal advection of seasonally warmed near-surface water under the ice shelf in summer [*Horgan et al.*, 2011].

[14] Tidal currents in high-latitude oceans tend to be fairly barotropic because of the weak stratification, simplifying models to the depth-averaged shallow water momentum and volume conservation equations based on *wct* [*MacAyeal*, 1984; *Robertson et al.*, 1998]. However, three processes complicate prediction of the contribution of tides to the total currents influencing thermodynamic exchanges at the ice base: critical latitude effects [*Makinson et al.*, 2006; *Robertson et al.*, 2001], generation of topographic vorticity waves (TVWs [e.g., *Cartwright*, 1969; *Middleton et al.*, 1987; *Padman and Kottmeier*, 2000]), and rectified flows [*MacAyeal*, 1985a]. For LCIS, which is several degrees away from the critical

latitudes for any tidal harmonics, we regard TVWs and rectified flows as the most significant sources of uncertainty in our ability to quantify tidal effects beneath LCIS.

[15] The mechanism that causes TVW amplification is essentially the same as for coastal-trapped waves [e.g., *Gill and Schumann*, 1974]; that is, the forced across-slope displacement stretches or shrinks the water column, resulting in a restoring force from the change in vorticity. The dispersion characteristics of TVWs in an unstratified ocean are sensitive to cross-slope topographic variation at fairly small length scales [e.g., *Middleton et al.*, 1987]. For typical Antarctic conditions of a deep continental shelf (~500 m) adjacent to an abyssal plain, the maximum frequency of a TVW is close to diurnal and, at these frequencies, the group velocity (i.e., the speed at which energy can propagate along slope) is close to zero. Thus, a mechanism exists to excite a TVW from the background diurnal tide, with only slow radiation of this energy away from the generation site. We will refer to these waves as diurnal topographic vorticity waves, or DTVWs. Energetic DTVWs have been identified in data in many high-latitude regions including the Arctic [*Hunkins*, 1986; *Padman et al.*, 1992] and the Antarctic [*Middleton et al.*, 1987; *Padman and Kottmeier*, 2000] and have been shown to increase diurnal currents by fivefold to tenfold off Vancouver Island [*Thomson and Crawford*, 1982]. *Padman et al.* [2009] observed and modeled DTVWs at the Ross Sea shelf break, where instantaneous current speeds exceed 1 m s^{-1}. The amplitudes and phases of DTVWs along the continental slope can vary rapidly over distances comparable to the slope width [*Middleton et al.*, 1987].

[16] Tidal rectification arises through nonlinearities associated with spatial gradients in friction, mean shear, and tidal coefficients, all of which are increased in the presence of topographic gradients [*Loder*, 1980; *Robinson*, 1981]. Rectified flows in an Eulerian frame (as would be measured at a mooring) can be of order 10% of the magnitude of the oscillatory tidal flows; the Lagrangian (particle following) mean flow can be up to ~15% [see *Padman et al.*, 1992]. The large spatial gradients of tidal coefficients in DTVWs imply a contribution to tidal rectification [see *Padman et al.*, 2009, Figure 10], such that we expect regions with strong DTVWs to also support a tidal contribution to mean circulation.

2.2. Larsen C Ice Shelf

[17] LCIS is the largest ice shelf on the Antarctic Peninsula, with an area of ~50,000 km^2 [*Cook and Vaughan*, 2010]. During the last several decades, the Antarctic Peninsula has experienced very rapid climate change [*Comiso*, 2000; *Skvarca et al.*, 1998, 1999; *Vaughan and Doake*, 1996] and significant retreat of ice shelves [*Cook and Vaughan*, 2010]. Portions of LCIS have experienced recent surface lowering [*Shepherd et al.*, 2003; *Zwally et al.*, 2005; *Fricker and Padman*, 2012] that may have been caused by firn compaction [*Holland et al.*, 2011], accelerated basal melting [*Shepherd et al.*, 2003], or both. Although LCIS is currently considered stable [*Cook and Vaughan*, 2010; *Jansen et al.*, 2010], its stability is attributed to marine ice accretion [*Jansen et al.*, 2010; *Khazendar et al.*, 2011], which may diminish if ocean temperatures rise [*Holland et al.*, 2009].

[18] The possibility that LCIS might follow its northern neighbors and collapse within the next century [*Scambos et al.*, 2003; *Shepherd et al.*, 2003] has motivated many
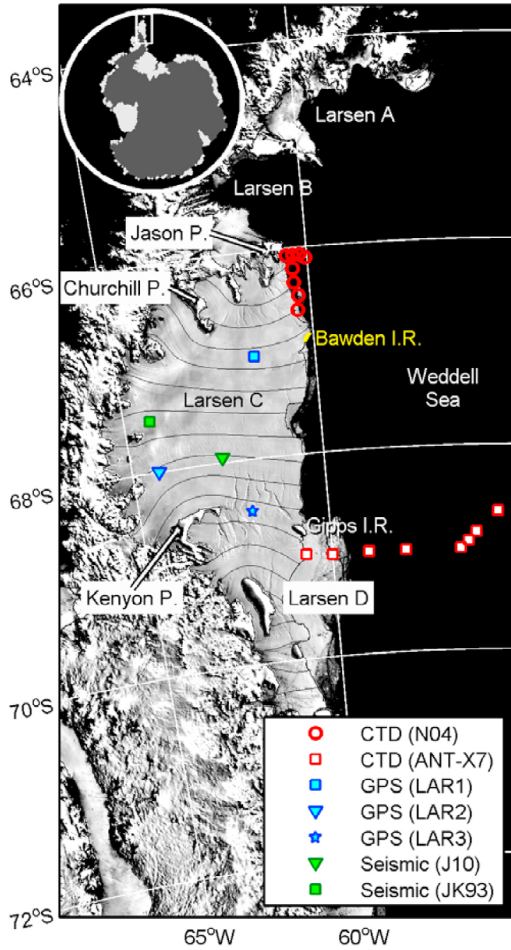
Figure 1. Location map for Larsen C Ice Shelf showing data sources used to define model geometry and hydrography. The Bawden Ice Rise, indicated by yellow, was not included in our model geometry. CTD stations include those reported by *Nicholls et al.* [2004] (N04) and *Bathmann et al.* [1994] (ANT-X7). GPS ice elevation data (LAR1, LAR2, LAR3) are described by *King et al.* [2011]. Seismic surveys from *Jarvis and King* [1993] (JK93) and *Jansen et al.* [2010] (J10) provided local measurements of ice and firn density profiles in addition to seabed depth and water column thickness. The black flow lines on the ice shelf are based on recent interferometric synthetic aperture radar velocity measurements of ice flow (described in section 2 of the auxiliary material).

recent field programs and modeling studies. Despite this activity, however, the *wct* under LCIS, and even the bathymetry (*D*) of the open continental shelf seaward of the LCIS ice front [*Luckman et al.*, 2010], remain poorly known. In addition, few hydrographic measurements exist to constrain the properties of the ocean water entering and leaving the sub-ice-shelf cavity. The locations of relevant hydrographic profiles are shown in Figure 1. Tide height ranges are significant, with the standard deviation of tide height being >1 m under LCIS [*Padman et al.*, 2002]; however, there are no measurements of tidal currents near LCIS, and we rely on barotropic tide models to estimate that tidal current speeds under LCIS may be large relative to the

thermohaline-only plume speeds of less than ~0.05 m s^{-1} [*Holland et al.*, 2009].

3. Model Configuration

[19] We investigate the three-dimensional ocean circulation beneath LCIS using the hydrostatic, primitive equation Regional Ocean Modeling System, version 3.2 (ROMS3.2) [*Shchepetkin and McWilliams*, 2009]. ROMS3.2 incorporates a terrain following (σ) coordinate that stretches the vertical coordinate depending on *wct*, thus providing higher vertical resolution in the dynamically important continental shelf region including the sub-ice-shelf cavity. Our version of the model has been slightly modified from the repository version to include ice shelf thermodynamic forcing (described below). We summarize the model parameters and setup specifications in Table 1.

[20] Efforts are presently underway to develop a frazil ice formation model for ROMS (B. Galton-Fenzi, personal communication, 2010), but this parameterization was not available for the present study. In our study, water that is colder than the in situ freezing point will result in heat and salt fluxes that are representative of freezing onto the ice shelf base. The effect of frazil ice would be to contribute more ice crystals to freezing and to enhance the buoyancy of the meltwater plume. However, the added buoyancy-driven flow given by frazil formation is likely negligible compared to overall plume speeds [*Galton-Fenzi*, 2009; P. Holland, personal communication, 11 August 2011]. An idealized cavity study described by *Galton-Fenzi* [2009] demonstrates a ~20% reduction in basal melting with the addition of frazil ice, although it is unclear how results from this idealized cavity would translate to realistic LCIS geometry.

3.1. Thermodynamic Forcing

[21] Thermodynamics at the interface between the ocean and ice shelf follows the three-equation approach described by equations (1), (2) and (5) of *Holland and Jenkins* [1999]. The melt rate w_b represents a change in ice draft (h_{draft}) over time; however, h_{draft} is maintained constant throughout each run. We differ from the *Holland and Jenkins* [1999] approach by using the scalar transfer coefficients described by *McPhee* [2008] and *Sirevaag* [2009]. We also simplify equation (2) of *Holland and Jenkins* [1999] with the assumption that the thermal conductivity within the ice shelf and the associated heat flux through the ice are negligible (i.e., the ice shelf is a perfect insulator, so that $Q_I^T = 0$). With this assumption, the kinematic heat flux (Q_o^T) and salt flux (Q_o^S) through the ocean's surface mixed layer is balanced by the thermodynamics of melting or freezing at the ice shelf base according to

$$Q_o^T = -\frac{L}{c_{pw}} w_b \tag{1}$$

$$Q_o^S = -S_b w_b, \tag{2}$$

where *L* is the latent heat of fusion, c_{pw} is the heat capacity of water, w_b is the isostatically adjusted vertical velocity at the top of the boundary layer, and S_b is the salinity at the ice-ocean interface. The value w_b is equivalent to the freshwater

Table 1. Parameter Definitions Used in the Numerical Model and Abbreviations Adopted in This Paper

Parameter	Symbol	Units	Value
Ocean heat flux	Q_o^T	°C m s^{-1}	
Heat flux through ice shelf	Q_i^T	°C m s^{-1}	0
Specific heat capacity (ocean)	c_{pw}	J kg^{-1} °C^{-1}	3985
Latent heat	L	J kg^{-1}	3.34×10^5
Meltwater equivalent for basal melt rate	w_b	m s^{-1}	
Ice density	ρ_i	kg m^{-3}	920
Mixed layer ocean density	ρ_o	kg m^{-3}	
Drag coefficient	C_d		2.5×10^{-3}
Thermal exchange coefficient	α_h		5×10^{-3}
Double diffusion ratio	R		33
Mixed layer ocean temperature	T_o	°C	
Initial ocean potential temperature	θ_0	°C	
Temperature of the ice at the ice-ocean interface (equivalent to the freezing point temperature)	T_b	°C	
Salinity of ice at the ice-ocean interface	S_b		
Mixed layer ocean salinity	S_o		
Ice elevation above sea level	h_{elev}	m	>0
Ice draft below mean sea level	h_{draft}	m	<0
Total ice thickness	$H = h_{\text{elev}} - h_{\text{draft}}$	m	>0
Sea floor depth	D	m	>0
Water column thickness	wct	m	>0
Time-averaged barotropic tidal current speed	U_{tide}	m s^{-1}	
Residual barotropic velocity vector	$\mathbf{u_{res}}$	m s^{-1}	

volume flux and is calculated from the change in ice thickness due to melt ($\partial H/\partial t$) as $w_b = -(\rho_i/\rho_o)(\partial H/\partial t)$, where ρ_i and ρ_o are the densities of the ice and ocean, respectively.

[22] Both Q_o^T and Q_o^S at the ice-ocean interface are functions of the friction velocity (u_{*o}), and the salt and temperature differences between the ice-ocean interface (S_b, T_b) and the ocean's mixed layer properties (S_o, T_o):

$$Q_o^T = \alpha_h u_{*o} (T_b - T_o) \qquad (3)$$

$$Q_o^S = \alpha_s u_{*o} (S_b - S_o). \qquad (4)$$

[23] Equation (3) introduces α_h as a thermal exchange coefficient [McPhee, 2008; Sirevaag, 2009]. This thermal exchange coefficient assumes the use of the interfacial salinity (S_b), rather than mixed layer salinity (S_o), to calculate the interfacial temperature (T_b). The saline exchange coefficient α_s is related to α_h by a double diffusion factor, R, such that $\alpha_s = \alpha_h/R$. At the time of this study, the available research with which to inform our choice of the double diffusion factor was from Arctic sea ice studies [e.g., Sirevaag, 2009; McPhee et al., 2008]. We chose $R = 33$ following Sirevaag [2009]. McPhee et al. [2008] suggest $R = 35–70$. The actual strength of double diffusion beneath LCIS is unknown; however, observations beneath Ronne Ice Shelf [Jenkins et al., 2010] suggest $R \approx 35$.

[24] A common approach to parameterizing the surface heat and salt fluxes in equations (3) and (4) is to represent $\alpha_h u_{*o}$ and $\alpha_s u_{*o}$ with constant thermal and saline exchange velocities, γ_T and γ_S [e.g., Holland and Jenkins, 1999]. These parameterizations are equivalent to assuming a uniform friction velocity at the ice-ocean interface. In order to assess the consequence of this assumption, we ran one model case with constant γ_T and γ_S (which we refer to as the constant γ_T case, Table 3) to compare with the cases that utilize the parameterization given by equations (3) and (4).

[25] We calculated u_{*o} in equations (3) and (4) from a surface quadratic stress such that $u_{*o}^2 = C_d |\mathbf{u}|^2$ with drag coefficient of $C_d = 2.5 \times 10^{-3}$ and velocity $\mathbf{u}$ taken from the surface σ level. We assume the surface mixed layer can be represented by the surface σ level and use these values of temperature and salinity for T_o and S_o. The value of T_b is approximated by the freezing point temperature, which we calculate following Foldvik and Kvinge [1974]:

$$T_b = 9.39 \times 10^{-2} - 5.7 \times 10^{-2} S_b + 7.641 \times 10^{-4} h_{\text{draft}}, \qquad (5)$$

where $h_{\text{draft}} < 0$. Equation (5) demonstrates the pressure dependence of w_b that is introduced by h_{draft}. We estimate S_b by combining the heat and salt fluxes given by equations (3) and (4) with equation (5) and solving for S_b. For the actual heat and salt fluxes into the top layer of the ocean model, we augment (3) and (4) to include the meltwater advection term described by Jenkins et al. [2001]. Values of parameter choices are provided in Table 1.

[26] Examples of similar applications in isopycnal coordinate system models are described by Holland and Jenkins [1999], Little et al. [2008, 2009], and Makinson et al. [2011]. A z coordinate model example is presented by Losch [2008]. More examples of applications using the ROMS model are given by Dinniman et al. [2007, 2011] and Galton-Fenzi [2009]. Additional σ coordinate model applications are provided by Grosfeld et al. [1997] and Beckmann et al. [1999]. A "plume model" approach, which assumes a nondynamic ocean beneath the ice shelf plume, is used by Holland and Feltham [2006], Payne et al. [2007], and Holland et al. [2007, 2009].

3.2. Model Grid and Domain

[27] The domain for simulations presented in this paper incorporates the portion of the Antarctic Peninsula (AP) that is shown in Figure 2. Our grid's node spacing is 2 km in the horizontal with 21 σ levels, the latter chosen to resolve the
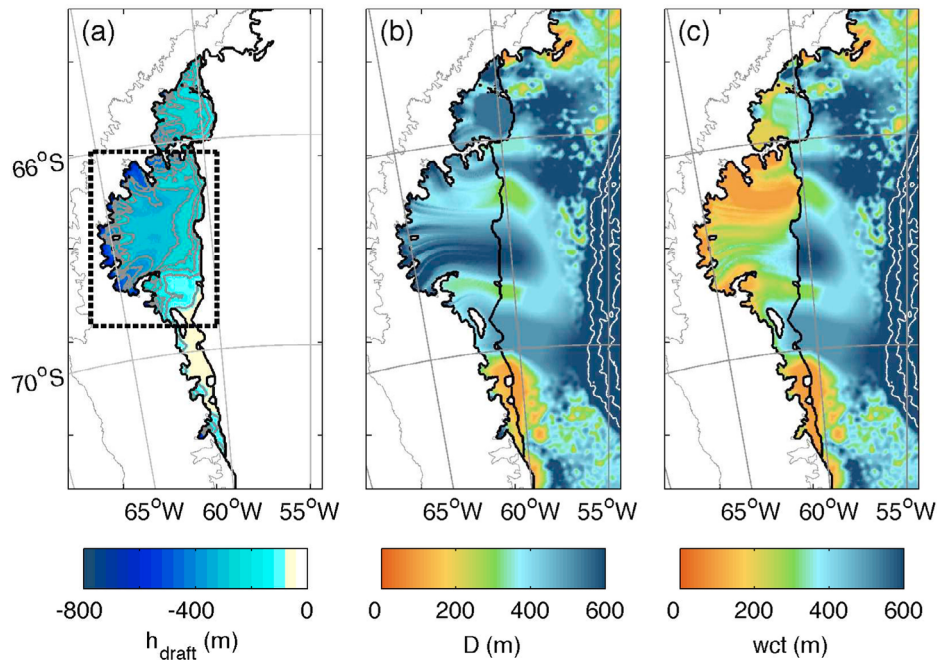
Figure 2. (a) Ice draft (h_{draft}) used for all simulations presented in this paper. The black lines represent the land mask and the ice shelf fronts used in our model. The thick gray lines are 50 m contour intervals of h_{draft}. The ice shelf within the dashed rectangle indicates the area that we refer to as LCIS and is the domain used to estimate LCIS-averaged values; this rectangle also shows the graphics boundary used in Figures 3, 5, 6, 7, and 8. (b) Bathymetry (D) used in all model runs except for the 350 m case. Isobaths $D = 1000$, 1500, and 2000 m are shown with white contours. (c) Water column thickness (wct) used for all simulations presented in this paper, with the exception of the 350 m case. Isobaths are the same as in Figure 2b. The thin gray outline mapping of the peninsula in Figures 2a–2c is not used in our model simulations but is shown here to provide regional context.

sub-ice-shelf surface mixed layer. Grids for ice draft (h_{draft}, see section 3.2.1) and bathymetry (D, see section 3.2.2) are poorly constrained in many areas of our model domain. Given the importance of wct on tide predictions (section 3.2.3), we attempted to create a realistic map of h_{draft} with two plausible options for D under LCIS. In creating and working with these maps, however, we recognized that the very large remaining uncertainties in geometry had a significant impact on w_b; thus, we consign the detailed description of grid development to the auxiliary material and focus here on describing the relevant features of the resulting maps and their inherent uncertainties.

3.2.1. Model Ice Draft (h_{draft})

[28] Our estimated ice draft, based on satellite radar altimetry for epoch 1994–1995, varies from ∼900 m at the grounding line (assumed to be stationary in our models) to ∼100 m at the ice shelf front, with an average value of ∼275 m (Figure 2a). The principal errors in converting ice elevation to h_{draft} arise from uncertainty in the density and thickness of the firn layer. A common approach to accounting for firn properties is to define a firn depth correction (Δh) obtained from measurements or models [see, e.g., *van den Broeke et al.*, 2008]. For LCIS, *Holland et al.* [2011] suggested a firn depth correction of between 0 and 20 m, assuming dry firn. In the northern LCIS, however, the firn is likely wet, suggesting a firn density correction error of 0 to 8 m, based on Figure 1 of *Holland et al.* [2011]. An 8 m

difference in firn density correction would amount to ∼80 m ice draft uncertainty in the northern LCIS. *Holland et al.* [2009] cited error in ice thickness measurements from airborne radio echo sounding on the order of 10 m. These data were used by *Holland et al.* [2009] to constrain ice draft estimates from BEDMAP [*Lythe et al.*, 2001] with the likely consequence of greatly reducing the error from firn density correction in their study. Our study relies on direct observations of firn depth and a representation of the latitudinal variations in firn density described by *Holland et al.* [2009] (see auxiliary material for details). Additional to the firn density error is an error from the uncertainty in the density of the marine ice that accumulates in bands in some regions of LCIS [*Holland et al.*, 2009].

3.2.2. Model Seabed Bathymetry (D)

[29] Our open ocean model bathymetry (Figure 2b) is interpolated from the grid for the CATS2008 tide model. This tide model utilizes data from the 2008 General Bathymetric Chart of the Oceans (GEBCO-2008 [*Hall*, 2006]) and the *Smith and Sandwell* [1997] global topography (TOPO12.1). The relatively smooth inner continental shelf seaward of LCIS reflects regions where the GEBCO-2008 gridded bathymetry is used while the rougher bathymetry further offshore is derived from TOPO12.1. Derivation of the estimated seabed bathymetry under LCIS is explained in auxiliary material.

[30] Our map of D under LCIS is qualitatively similar to a recent grid developed from airborne gravity measurements

Table 2. Amplitude and Phase Values for the M_2 Tidal Constituent at Three Locations on LCIS[a]

	LAR1		LAR2		LAR3	
	[−67.01°N, 298.49°E]		[−68.00°N, 295.71°E]		[−68.50°N, 298.00°E]	
	Amplitude (m)	Phase (deg)	Amplitude (m)	Phase (deg)	Amplitude (m)	Phase (deg)
GPS	0.8976	250.9100	0.9654	245.2500	0.8854	242.1500
$1 \times wct$	0.9371	255.3083	1.1030	248.5347	0.9288	240.7234
$2 \times wct$	0.8918	251.3053	0.9760	245.6854	0.8847	241.3558
$3 \times wct$	0.8710	249.9547	0.9292	245.2029	0.8641	241.7842
ROMS3.2	0.7344	246.1846	0.7995	238.5865	0.7139	236.2718
CATS2008a	0.8973	255.3183	1.0386	248.7382	0.8909	240.8185

    [a]These locations are selected to compare with the GPS data from *King et al.* [2011], the locations of which are shown in Figure 1. GPS data shown. The $1\times$ to $3\times$ *wct* test cases use the forward-only (no data assimilation) mode of the barotropic tide model CATS2008a and uniformly multiply *wct* by a factor of 1–3. The $1 \times wct$ test case differs from the CATS2008a case in that the latter utilizes data assimilation; however, the bathymetry is the same for each of these two cases.

[*Cochran and Bell*, 2012]. Both grids show much shallower bathymetry under the northern half of LCIS. The GEBCO-2008 product imposes a roughly semicircular bank over the open continental shelf; however, there are few available in situ depth data east of the LCIS ice front [see *Luckman et al.*, 2010, Figure 1] and no airborne gravity measurements to confirm this feature.

3.2.3. Model Water Column Thickness (*wct*)

[31] The *wct* represents the distance from the seabed to the base of the ice shelf; it is equivalent to D offshore of the ice shelf and to $D + h_{draft}$ beneath the ice shelf (where $D > 0$ and $h_{draft} < 0$). Our base case grid *wct* (Figure 2c), used for most runs reported in this paper, shows small *wct* in the northern half of LCIS where D is shallow, and a region of large *wct* in the southern portion of LCIS north of Gipps Ice Rise. Errors in *wct* arise from errors in h_{draft} (primarily due to uncertainties in the densities and thicknesses of firn and marine ice) and the larger uncertainties in D under and adjacent to LCIS. However, the general agreement between our grid of D and that developed by *Cochran and Bell* [2012] suggests that our grids will contain the principal geometric features influencing LCIS tides and basal melting.

[32] Tidal analyses of recently acquired ice surface elevation time series from GPS receivers on LCIS [*King et al.*, 2011] provide an opportunity to assess the general accuracy of our *wct* map. Following the method used by *Galton-Fenzi et al.* [2008] for Amery Ice Shelf, we investigate how changing *wct* under LCIS in a barotropic tide model affects the misfit between modeled and GPS-measured tide heights. The model used for this assessment is a regional subset of the CATS2008 inverse tide model. We ran the model for three *wct* grids (explained below) in forward mode (i.e., with dynamics but no data assimilation) but with open boundary conditions taken from the CATS2008 inverse tide model. This approach allowed us to assess how changes in *wct* affect the accuracy of the tide predictions judged relative to unassimilated data (the GPS records from *King et al.* [2011]). The LCIS-averaged *wct* ($\langle wct \rangle_{LCIS}$) for CATS2008 is ~133 m, significantly less than $\langle wct \rangle_{LCIS} = 211$ m for our base case grid. We refer to the standard CATS2008 grid as "case $1 \times wct$"; two other test grids were constructed by multiplying the CATS2008 *wct* under LCIS by two and three (cases $2 \times wct$ and $3 \times wct$, respectively). The tests therefore span a range of $\langle wct \rangle_{LCIS}$ from 133 to 399 m, encompassing the value of $\langle wct \rangle_{LCIS} = 211$ m for our base case geometry.

[33] We compared the observed tide amplitude variations from each of three GPS stations (locations shown on Figure 1) to the three modeled cases described above (Table 2), focusing on the largest semidiurnal tidal constituent M_2. We used M_2 because its dynamical behavior as a Kelvin wave is simpler than the diurnal tides (O_1 and K_1), which contain significant energy as DTVWs (see section 2.1) and are very sensitive to small-scale gradients in *wct*. The comparisons (Table 2) show that the $2 \times wct$ run most closely matches the GPS measured amplitude and phase for M_2 at all three locations, suggesting that the true value of $\langle wct \rangle_{LCIS}$ is in the range of 200–300 m. The spatial variability of the *wct* remains unknown.

[34] The ROMS3.2 three-dimensional model presented here produces slightly weaker tides under LCIS than the barotropic runs based on CATS2008 (see Table 2). We discuss possible reasons for this in section 3.3.1.

3.3. Model Forcing

[35] Thermohaline exchange between the ocean and ice shelf is dependent on the temperature difference between the ice and the adjacent mixed layer, and the mixed layer current speed as a source of turbulence both at the ice base and at the interface with the underlying ocean (section 3.1). Several factors external to the cavity can influence the water mass properties and circulation within the cavity, including: sea ice formation, winds, general ocean circulation (the large-scale Weddell Gyre), and tides. In this paper, we focus on the influence of tides, as described below. However, we also carried out a single test of sensitivity to initial ocean potential temperature θ_0, since the *Holland et al.* [2009] plume model of LCIS suggested that quite small changes in θ_0 could profoundly alter the magnitude and spatial distribution of basal melting and refreezing. We choose a "base case" setup and compare our sensitivity tests to these results. Details of the base case grid were described in section 3.2 and other specifications are discussed in sections 4.2. We also provide an overview of model simulations and forcing characteristics in Table 3.

3.3.1. Tides

[36] For all cases involving tidal forcing, we forced the open boundaries to the north, south, and east with tidal constituents extracted from CATS2008. The four most energetic constituents are M_2 (period 12.42 h), S_2 (12.00 h), K_1 (23.96 h), and O_1 (25.82 h). Together, they account for most of the energy in the full tidal solution. There are

Table 3. An Overview of Tide Forcing Scenarios for the Different Runs Shown in This Paper

Reference Name	Tidal Constituents	Amplification Factor	θ_0	Other
Base	M_2, S_2, K_1, O_1	1	$-1.7°C$	10 year plus 180 day run 30 day average (<10 years) 2 day average (>10 years)
Cold case	M_2, S_2, K_1, O_1	1	$-1.9°C$	600 day run
350 m	M_2, S_2, K_1, O_1	1	$-1.7°C$	Imposed min(D) = 350 m in LCIS 10 year plus 180 day run 30 day average (<10 years) 2 day average (>10 years)
No thermo	M_2, S_2, K_1, O_1	1	$-1.7°C$	40 day run 2 h average output no thermodynamics
$0.5 \times$ tides	M_2, S_2, K_1, O_1	0.5	$-1.7°C$	600 day run 30 day average output
$0.75 \times$ tides	M_2, S_2, K_1, O_1	0.75	$-1.7°C$	600 day run 30 day average output
$2 \times$ tides	M_2, S_2, K_1, O_1	2	$-1.7°C$	600 day run 30 day average output
$M_2 + S_2$	M_2, S_2	1	$-1.7°C$	400 day run 2 day average output
$K_1 + O_1$	K_1, O_1	1	$-1.7°C$	400 day run 2 day average output
min u_{*o}	closed boundaries	NA[a]	$-1.7°C$	$\min(u_{*o}) = 0.0001$ m s^{-1} 400 day run 2 day average output
Constant γ_T	closed boundaries	NA[a]	$-1.7°C$	$\gamma_T = 1 \times 10^{-4}$ m s^{-1} $\gamma_S = 5.05 \times 10^{-7}$ m s^{-1} 400 day run 2 day average output

[a]NA, not applicable.

some cases in which we closed the boundaries or forced the model with a subset of the diurnal and semidiurnal tides. When using open boundaries, the tidal forcing was applied with Flather boundary conditions for the barotropic velocity [*Flather*, 1976] and Chapman boundary conditions for the free surface height [*Chapman*, 1985]. These conditions allow the barotropic velocity and surface elevations that deviate from exterior values to radiate out at the speed of external gravity waves. We applied 3D momentum and tracer diffusion at the boundaries and ramped the tide forcing from zero to 100% over ~20 days. We amplified the horizontal eddy viscosity (A_h) and diffusivity (K_h) along the open boundaries by a factor of ten and decreased this amplification to the background levels within the interior using a cosine taper across a sponge perimeter 20 grid cells wide.

[37] Tide height amplitudes predicted by ROMS3.2 under LCIS are about 20% weaker than in the CATS runs (Table 2), consistent with reductions of both heights and currents in the open ocean portion of the domain. We attribute this change to the effect of a different *wct* under LCIS, which is a significant fraction of our total model domain area. Model open boundary conditions in ROMS3.2 compensate for the resulting errors in tidal amplitude and phase by modifying the tidal energy flux across the open boundaries. A new barotropic tide model that takes advantage of improved estimates of sub-ice-shelf *wct* will reduce this difference.

3.3.2. Hydrography

[38] Observations of the ocean properties in front of LCIS are limited to the locations shown in Figure 1. The most complete analysis of the hydrography adjacent to LCIS is

given by *Nicholls et al.* [2004], who observed potential temperatures ranging from about $-1.4°C$ to $-2.1°C$ on the continental shelf adjacent to LCIS. Using a Gade line extrapolation [*Gade*, 1979] from the temperature and salinity of the meltwater plume, *Nicholls et al.* [2004] concluded that the primary inflow to the LCIS sub-ice-shelf cavity is Modified Weddell Deep Water (MWDW) that flows onto the continental shelf, where it is cooled to the surface freezing point of $-1.9°C$ and salinized to 34.63 during the winter. During the summer, MWDW may be advected toward the ice shelf cavity and cause the continental shelf waters to warm up to $-1.4°C$, but the authors state that it is unclear whether this warmer source water enters the sub-ice-shelf cavity.

[39] *Holland et al.* [2009] used an ocean temperature of $-1.9°C$ to force a plume model experiment and compared these results to a "warm" case with inflow temperature of $-1.4°C$. Modeled LCIS-integrated mass loss estimates for these two runs were 15 Gt a^{-1} and 70 Gt a^{-1}, respectively. For comparison, the flow of ice across the grounding zone for Graham Land (the portion of the AP that is approximately north of the Kenyon Peninsula in Figure 1) is estimated from observations of interferometric synthetic aperture radar (InSAR) velocities and ice thicknesses at 20 and 49 Gt a^{-1} for 1996 and 2006, respectively [*Rignot et al.*, 2008]. Although LCIS is the largest ice shelf in this region, these ice flux estimates include the impact of accelerated ice stream velocities following the collapse of the Larsen A and B ice shelves in 1995 and 2002, respectively; hence, the *Rignot et al.* [2008] values should be upper limits on mass loss by basal melting of LCIS alone. For LCIS to be in mass balance, ice sheet outflow to LCIS is balanced by
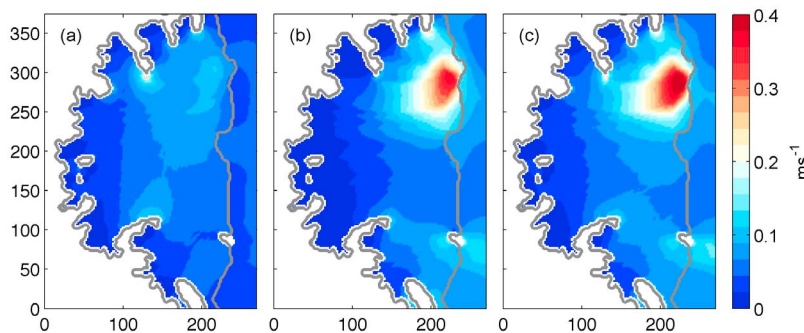
Figure 3. Major axis of the barotropic tidal ellipse for the largest semidiurnal and diurnal tide components (a) M_2 and (b) O_1. (c) The map of time-averaged barotropic tidal current speed (U_{tide}, equation (6)). All values are estimated from the last 30 days of a 40 day run with 2 h averaged output and no thermodynamic ice-ocean exchange. The x and y axes show distances in km.

calving or ice front advance, basal melt and accumulation, such that the lower modeled integrated melt rate from *Holland et al.* [2009] (associated with $\theta_0 = -1.9°C$) more closely approximates observed values.

[40] In this experiment, we follow *Holland et al.* [2009] by using initially homogeneous fields for ocean temperature and salinity. For most of our simulations we chose a θ_0 of $-1.7°C$ and a salinity of 34.65. This salinity value corresponds to the "cold case" plume model run by *Holland et al.* [2009] while temperature was chosen as a moderate value for the plausible range of $-1.9°C$ to $-1.4°C$ inflow temperatures. For one simulation, we set initial temperature to $-1.9°C$ to represent the best estimate of inflow temperature given by *Nicholls et al.* [2004] and the cold case of *Holland et al.* [2009]. For reasons explained in section 4.8, we believe that the colder case ($\theta_0 = -1.9°C$) is more consistent with available LCIS data; however, the warmer case provides a more robust melting signal for sensitivity studies.

3.4. Errors

[41] Here we summarize the primary sources of numerical errors in our simulations. More detail is provided in the auxiliary material.

[42] The ROMS3.2 σ level vertical coordinate system and staggered Arakawa C grid introduce conservative requirements of topographic variability to ensure model stability and general performance. The problem of numerical errors introduced by steep bathymetric slopes is exacerbated by the presence of the ice shelf base, which introduces a second sloping boundary to that of bathymetry. Therefore, a challenge in the present study was to create model grids that satisfied the conditions of model stability while also adequately resolving the sub-ice-shelf ocean boundary layer. To meet this challenge, we chose a sufficient number of levels (21) so that the maximum upper layer thickness under ice is about 20 m, smaller than the expected upper ocean boundary layer of about 50 m. In addition, we minimized the possibility of unrealistic spurious flows generated by baroclinic pressure gradient errors by smoothing the seabed bathymetry and ice draft grids to satisfy the Haney criterion [*Haney*, 1991] over most of the grid. The Haney criterion limits the vertical displacement of σ levels between adjacent grid cells to allow accurate interpolation of baroclinic pressure at

specific depths (see auxiliary material). We also imposed a minimum value of $wct = 100$ m prior to our final smoothing.

[43] We ran several tests to determine the optimum advection scheme and the minimum background values for viscosity and diffusivity required to prevent grid scale errors from growing with time. For all runs described in this paper we used the default advection schemes (fourth-order centered for tracers and vertical advection of momentum, and third-order upstream for horizontal advection of momentum) with a Mellor-Yamada 2.5 turbulence closure scheme for vertical mixing [*Mellor and Yamada*, 1974, 1982]. Minimum vertical eddy viscosity and diffusivity coefficients were $A_{z,min}$, $K_{z,min} = 5 \times 10^{-5}$ m^2 s^{-1} and 1×10^{-5} m^2 s^{-1}, respectively, and Laplacian horizontal mixing coefficients were $A_h = 5$ m^2 s^{-1} and $K_h = 1$ m^2 s^{-1}. Horizontal mixing is along σ levels for momentum and geopotential surfaces for tracers. A complete list of the model's C preprocessing options (referred to as "cppdefs") is provided in the auxiliary material.

4. Results

4.1. Tidal Current Distribution

[44] Tidal analyses of a model run with no thermohaline ice-ocean exchange indicate that the O_1 diurnal constituent generates the strongest tidal currents, with the largest values in the NE region of LCIS (Figure 3). Figures 3a and 3b show the spatial distribution of the magnitude of the barotropic tidal ellipses for the M_2 and O_1 constituents, respectively. The spatial pattern of K_1 currents is similar to O_1, but the mean magnitude is ~12% lower; likewise, S_2 currents resemble M_2 but their magnitude is, on average, 30% lower. The large barotropic currents in the NE region are dominated by the diurnal tides, even though the modeled diurnal tidal elevation amplitudes are smaller in this region than those of the semidiurnal tides (not shown). We attribute this enhancement to the generation of DTVWs (see section 2.1). The largest semidiurnal currents occur near the Churchill and Kenyon Peninsulas (Figure 3a) but are much weaker than the diurnal currents in the NE region (Figure 3b). Modeled tidal currents along the deep grounding line of the western LCIS are small; however, we imposed a minimum wct of 100 m (see section 3.4), so that actual tidal current speeds
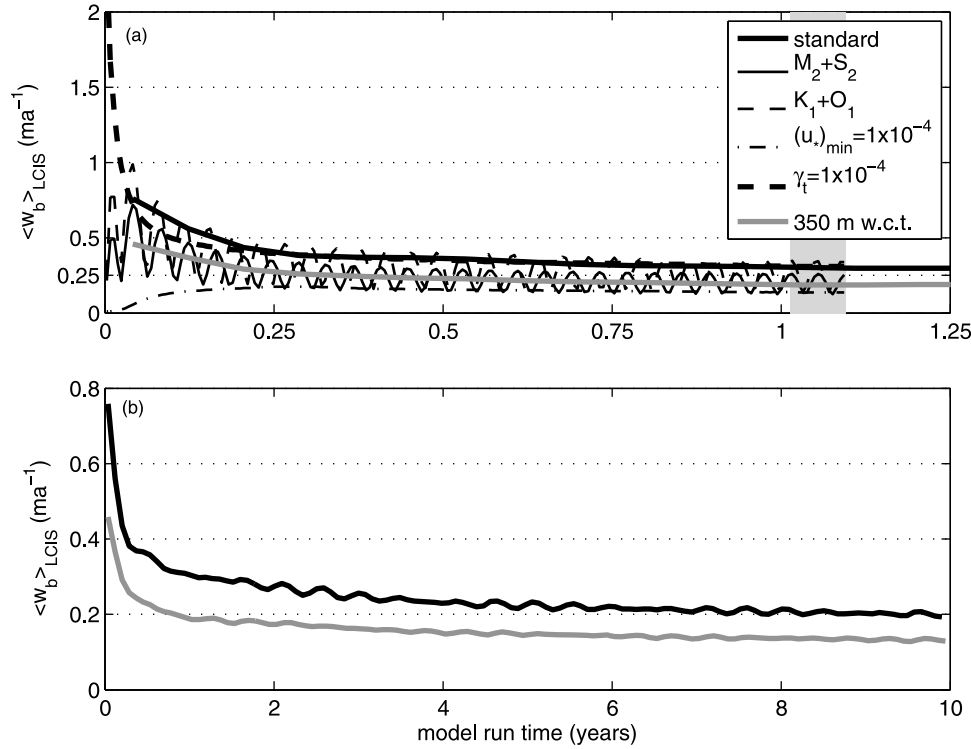
Figure 4. (a) Model run equilibrations as shown by melt rate averages for LCIS. The $K_1 + O_1$ and $M_2 + S_2$ runs output 2 day averages while all others output 30 day averages. The shaded gray region shows the time period over which results were averaged to yield melt rate maps shown in Figure 7. (b) Time history of LCIS 30 day averaged melt rate for the base case (black line) and 350 m case (gray line), showing convergence to approximate steady state after 10 years.

may be larger than in our model where true *wct* is less than 100 m.

[45] For simulations forced by multiple tidal constituents, we characterize the spatial variability of tidal currents by mapping the time- and depth-averaged tidal current speed U_{tide}, determined from

$$U_{\text{tide}} = \left\langle \sqrt{u_b^2 + v_b^2} \right\rangle_t, \qquad (6)$$

where $u_b(x, y, t)$ and $v_b(x, y, t)$ are orthogonal components of modeled, depth-averaged current and $\langle \rangle_t$ represents temporal averaging. This value represents a typical tidal current speed contributing to mixing near the ice-ocean interface. Figure 3c shows U_{tide} for our standard geometry (Figure 2) based on the last 30 days of our run with no ice-ocean thermodynamics ("no thermo" case in Table 3). The largest values of U_{tide} exceed 0.4 m s^{-1} in the northeast region of LCIS.

[46] The semidiurnal tides, M_2 and S_2, introduce a spring-neap cycle of modulation with period ~14.7 days; similarly, O_1 and K_1 produce a spring-neap cycle with period ~13.7 days. These two cycles beat together to produce a semiannual cycle with periodicity of ~183 days (e.g., Figure 4b). Tides will also be modulated by the ~18.6 year lunar node tide cycle, but we neglect this variation because our model run time is not sufficiently long. The lunar node modulation introduces an additional ~10% variability of amplitude in the northeastern LCIS region, as predicted by the CATS2008 barotropic tide model.

4.2. Base Case

[47] Our base case model (Table 3) has an initial uniform potential temperature of $\theta_0 = -1.7°C$ and $S_o = 34.65$ (see section 3.3.2). Boundary forcing was obtained from the M_2, S_2, K_1, and O_1 tidal constituents provided by CATS2008 (see section 3.3.1). This setup was run for 10 model years and the output was averaged over 30 day intervals (~2 spring-neap cycles). After completion, the base case was restarted to run for an additional 180 days with 2 day averaged output. For this extension run we also introduced a passive dye tracer beneath LCIS and Lagrangian floats at various depths and locations along the LCIS front.

[48] The spatial pattern of time-averaged w_b for the base case, averaged over the 180 day extension run, is shown in Figure 5a. A maximum value of ~2 m a^{-1} occurs in the NE region and is colocated with the region of largest time-averaged barotropic tidal speeds. As explained in section 4.1, these large current speeds are mainly due to the diurnal tides (Figures 3b and 3c). The time-averaged surface σ level velocity represents the thermohaline plume and is shown in Figure 5b. The plume speeds are greatest at the grounding line, along a band oriented NE through the midshelf region, along the ice front, and around the region of amplified melt.

[49] In the NE region, the combination of small *wct*, large spatial gradients of *wct* and associated large gradients in tidal currents provides the conditions required for generation of rectified tidal flows (see section 2.1). We evaluated the modeled Eulerian component of these rectified flows by
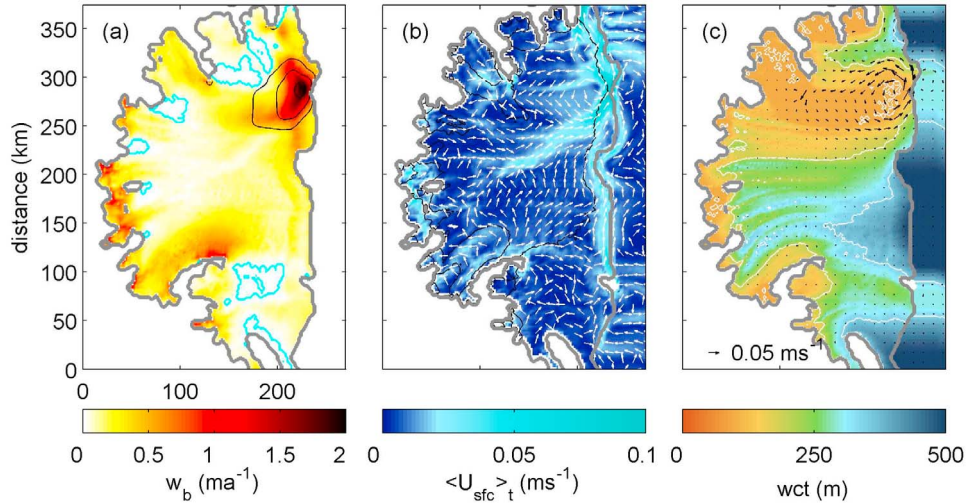
Figure 5. (a) Melt rate (w_b) for the base case averaged over the 180 day restart following the 10 year base run. Black contours show magnitude of the 30 day time-averaged barotropic current speed (U_{tide}, equation (6)), with contour intervals at U_{tide} = 0.2, 0.3, 0.4 m s^{-1}. Cyan contours indicate regions where $w_b < 0$ m a^{-1} in the base case, i.e., locations of marine ice accretion. (b) Thermohaline and residual circulation for the base case, represented by the magnitude of the 180 day time-averaged surface current ($\langle U_{sfc} \rangle_t$, color scale) with white unit vectors indicating direction. The black contours show ice draft at intervals of 600, 400, 300, and 200 m. (c) Water column thickness (*wct*) with white contours at 100, 200, and 350 m. The overlaying vectors show the residual barotropic circulation ($\mathbf{u_{res}}$, equation (7)), from the 30 day averages of the "no thermo" case. These vectors are shown for the 5 × 5 2-D boxcar filtered values described in section 4.2.

calculating, from the tide-forced run with no ice-ocean thermodynamics, the modeled time-averaged ("residual") barotropic velocity

$$\mathbf{u_{res}}(x,y) = (\langle u_b(x,y,t) \rangle_t, \langle v_b(x,y,t) \rangle_t), \qquad (7)$$

where u_b and v_b are defined in section 4.1. Values of $\mathbf{u_{res}}$ are noisy, associated with numerical errors at the grid-scale level in the model. We therefore used a 5 × 5 2-D boxcar filter to smooth $\mathbf{u_{res}}$ to resolve scales of ocean variability (~5δx, where $\delta x = 2$ km is the grid node spacing). The vector map of filtered $\mathbf{u_{res}}$ is shown in Figure 5c. About 1% of the values of the magnitude of $\mathbf{u_{res}}$ ($|\mathbf{u_{res}}|$) beneath LCIS are greater than 0.05 m s^{-1}. For grid cells where U_{tide} exceeds 0.05 m s^{-1}, the mean of the ratio $|\mathbf{u_{res}}(x, y)|/U_{tide}$ is ~0.05 with a standard deviation of ~0.06.

[50] As a comparison, a sensitivity case that neglects tidal forcing (see min u$_{*0}$ case in section 4.3) has a maximum value of the 30 day averaged, surface level velocity, after one year, of 0.01 m s^{-1}. Hence, $|\mathbf{u_{res}}|$ can be large relative to the thermohaline-only plume speeds under LCIS, implying that rectified barotropic tidal circulation may exert significant control on the transport of meltwater plumes under LCIS. Rectified tides may play an additional role of ventilating the sub-ice-shelf cavity [cf. *Makinson and Nicholls*, 1999]. We do not, in this paper, attempt to separate the effects of increased mixing and mean advection by rectified tides on the distribution and magnitude of w_b.

[51] Weaker local maxima in w_b are also found along the northern flank of Kenyon Peninsula and near the grounding zone under the western LCIS. Locations of augmented melt in the western margins of the ice shelf cavity correspond to the deepest points of the ice shelf draft. These regions are also the high-melt sites seen in the *Holland et al.* [2009] plume model. The modeled tidal currents are negligible in this region (Figure 3), and we attribute the augmented melt there to the pressure suppression of T_f.

[52] The base case predicts that meltwater will refreeze to the ice shelf base in a few small regions (Figure 5a). Most of these regions are toward the back of the LCIS cavity in regions where cold meltwater from the deep grounding zone is buoyantly forced upward to depths where the plume temperature becomes less than T_f. These locations are in general agreement with the onset of marine ice flow bands identified from signal quality in airborne radio echo sounding of *Holland et al.* [2009]; however, we reiterate that our model lacks the ability to create frazil ice within the water column, so that we cannot confirm the marine ice accumulation rates estimated by *Holland et al.* [2009].

4.3. Tide Forcing and *wct* Sensitivity

[53] Our analyses of GPS tidal data (section 3.2.3) suggest that the average *wct* for LCIS ($\langle wct \rangle_{LCIS}$) is ~250 m, compared to 211 m for our base model geometry (which was created using available data for ice elevation and bathymetry). Two point measurements of *wct* from seismic soundings (see Table 4) indicate local *wct* of 362 and 412 m. Based on these limited constraints, we created a second model geometry to investigate the potential influence of *wct* uncertainty by imposing a minimum *wct* of 350 m beneath LCIS, with a resulting $\langle wct \rangle_{LCIS}$ of 355 m (we refer to this as the "350 m case"). We did this by retaining the original map of h_{draft} and increasing D in order to enforce the minimum *wct* criteria, then resmoothing the grid to minimize pressure

Table 4. Estimates of *wct* From Seismic Data and an Aircraft Gravity Survey Compared to the Base Case Bathymetry and the CATS2008a Bathymetry[a]

Source	Mean *wct* (m)	Location A	Location B	Location C	Accuracy (m)
Base grid	211	284	294	100	unknown
CATS2008a	133	150	149	160	unknown
Cochran and Bell [2012]	376	336	315	151	
Bernd Kulessa[b]		412			1
Jarvis and King [1993]			362		

[a]Estimates of *wct* (m) from seismic data and an aircraft gravity survey compared to the base case bathymetry and the CATS2008a bathymetry. Location A is located at $-67.98°N$, $62.63°W$; it is produced by values averaged between $67.95°N$, $62.62°W$ and $68.00°N$, $62.64°N$ (B. Kulessa, personal communication, 2009). Location B refers to $67.50°N$, $64.33°W$. Location C refers to $66.92°N$, $60.56°W$ (within high melt region in the northeast LCIS). Locations A and B are shown, respectively, as J10 and JK93 in Figure 1. Location C is near LAR1 of Figure 1 and is situated within the region of high melt shown in Figure 5a.

[b]This value is averaged between $-67.95°N$, $62.62°W$ and $-68.00°N$, $62.64°N$ to yield J10 "location A" (B. Kulessa, personal communication, 16 June 2009).

gradient errors (discussed in section 3.4 and in the auxiliary material). As shown in Figure 6, this case significantly increases *wct* in the northern section of the ice shelf and reduces the tidal currents from the base case values (Figure 6b), primarily by diminishing the magnitude of diurnal components. The effect of this reduced tidal forcing is a decrease in the basal melt in the NE region by as much as 2.3 m a^{-1} (Figure 6c). We attribute this decrease to the removal of geometric conditions required for the excitation of DTVWs (sections 2.1 and 4.1).

[54] In order to further assess the sensitivity of the spatial distribution of LCIS basal melt rate to tidal forcing, we ran seven simulations in addition to the base and 350 m cases

described above (see Table 3). These are: $K_1 + O_1$, $M_2 + S_2$, min u_{*o}, constant γ_T, and three cases with scaled tidal forcing. The $K_1 + O_1$ and $M_2 + S_2$ cases separate the influences of diurnal and semidiurnal tides. The min u_{*o} case approximates the plume flow model reported by *Holland et al.* [2009]; however, significant differences between the models limit direct comparison. The constant γ_T case represents a common approach to simplified representation of currents due to unresolved processes (such as tides) in models (see section 3.1). The three simulations with scaled open boundary tide forcing were run to represent a range of tidal currents under LCIS that incorporate the estimated uncertainties due to model limitations.

[55] Most runs are 400–600 day simulations, determined by available computational resources; however, the base and 350 m cases are 10 year simulations. The time series of modeled ice shelf averaged w_b rates indicate that most adjustment to forcing occurs in the first few simulated months (Figure 4a), although the value for the base case declines a further ~30% from 0.30 to 0.21 m a^{-1} from model year 1 to year 10 (Figure 4b).

[56] In Figure 7, we compare the maps of w_b from the base case with the 350 m case and the first four cases described above, using 30 day time-averaged values from around 365 days of model run time. The 350 m *wct* case tests the influence of *wct* on w_b. This case uses the same tidal forcing as in the base case; however, the resulting tidal currents (not shown) under LCIS are much lower amplitude. This reduction in tidal currents effectively removes the amplified basal melt in the NE region (Figures 7a and 7b). Away from the NE region, these two cases produce equivalent predictions. The $K_1 + O_1$ case captures most of the variability of $w_b(x, y)$ in the base case (compare Figures 7a and 7c). The $M_2 + S_2$ case (Figure 7d) is similar to the 350 m case, with strongest melt along the Churchill and
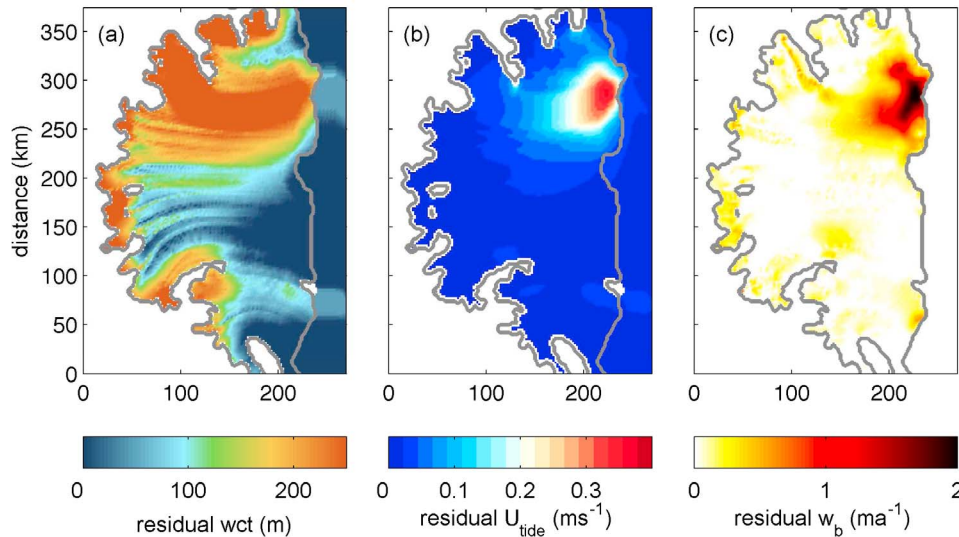

Figure 6. (a) Difference between *wct* for the 350 m and base cases (*wct*(350 m) − *wct*(base)). (b) Difference between time-averaged tidal current speed for the 350 m and base cases (positive values imply that base case currents are stronger than in the 350 m case). (c) Difference in w_b between the base and 350 m cases (i.e., w_b(base) − w_b(350 m)). Positive values indicate more melt in the base case than in the 350 m case.
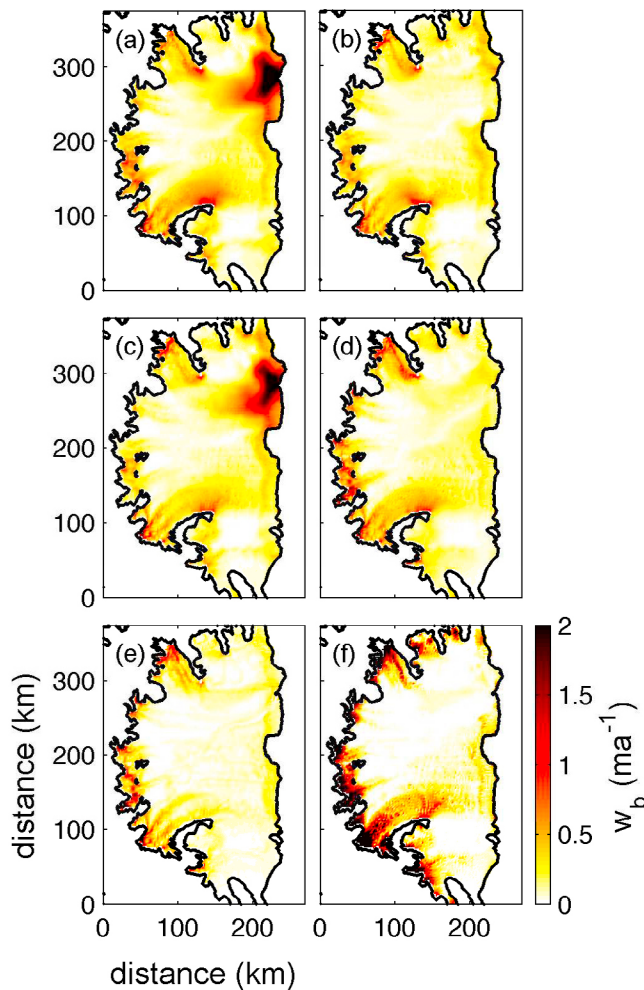
Figure 7. Melt rate (w_b) averaged over 30 days at $\sim$1 year of model run time for cases (a) base, (b) 350 m, (c) $K_1 + O_1$, (d) $M_2 + S_2$, (e) min u_{*o}, and (f) constant γ_t (see Table 3). The black contours show the ice shelf boundaries applied in our model domain. The maximum melt rate in the NE quadrant for the base case shown in Figure 7a is $\sim$3 m a^{-1}.

Kenyon peninsulas and the deep grounding lines in the western LCIS; the large melt signature in the NE is absent.

[57] The min u_{*o} case was uniformly initialized with a minimum $u_{*o} = 1 \times 10^{-4}$ m^2 s^{-1} that could increase as the thermohaline circulation developed. This case most closely approximates a plume model approach. The spatial pattern of w_b for this run (Figure 7e) is very different from the base case. Most basal melt for the min u_{*o} case is concentrated near the grounding zone while all other non-pressure-dependent melt is negligible.

[58] The constant γ_T case is equivalent to assuming a total current (tidal plus thermohaline) speed that is uniform everywhere under the ice shelf. We chose values of $\gamma_T = 1 \times 10^{-4}$ m^2 s^{-1} and $\gamma_S = 5.05 \times 10^{-7}$ m^2 s^{-1} to be consistent with several prior model studies [e.g., *Hellmer and Olbers*, 1989; *Holland and Jenkins*, 1999; *Beckmann et al.*, 1999; *Dinniman et al.*, 2007]. This parameterization results in strong melt at the grounding zone with little melt

elsewhere (Figure 7f). Since our modeled tidal currents are low over much of LCIS including along the deep grounding line in the western LCIS (Figure 3), the constant γ_T case overestimates the current speeds for much of the ice shelf and produces w_b values that are much higher than in the base case in the grounding zone.

4.4. Sensitivity of w_b to Ocean Temperature

[59] For one run ("cold case", see Table 3), θ_0 was set to $-1.9°C$, the approximate surface freezing point for water at the specified salinity of $S_o = 34.65$. All other factors, including geometry and tide forcing, are the same as for the base case. The spatial structure of the map of w_b for the cold case (Figure 8) is similar to that for the base case but with a reduction of 67% in LCIS-averaged melt rate. This result demonstrates that the strong dependence of melt rate on ocean temperature found in the plume-only model by *Holland et al.* [2009] is also true for our tide-forced models.

4.5. Basal Melt Relative to Ice Draft

[60] The primary differences in spatial heterogeneity of w_b for the major model runs are characterized by averaging w_b into 50 m ranges of h_{draft} (Figure 9a) and calculating area-integrated ice volume loss rates binned into the same h_{draft} ranges (Figure 9b). The base case results show highest values of bin-averaged w_b ($\sim$1.5 m a^{-1}) under thick ice near the grounding line (Figure 9a); however, most net volume loss is predicted under the much more extensive regions of shallower ice near the ice front (Figure 9b). Consistent with Figures 7a and 7c, the distribution of net volume loss for the $K_1 + O_1$ case is close to that for the base case.

[61] The constant γ_T case results show much larger values of LCIS-averaged w_b for $h_{draft} < -300$ m (Figure 9a). Values near the deep grounding lines are $\sim$4 times greater than in the base case. The area-integrated values for the constant
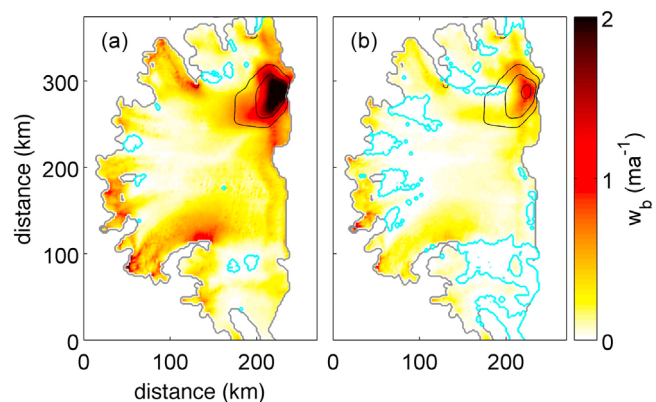

Figure 8. (a) Similar to Figure 5a: Melt rate (w_b) for the base case averaged over 30 days at $\sim$1 year of model run time. Black contours show magnitude of the 30 day time-averaged barotropic current speed (from the "no thermo" case in Table 3), with contour intervals at $\langle |\mathbf{u_b}| \rangle_t =$ 0.2, 0.3, 0.4 m s^{-1}. Cyan contours indicate regions where $w_b < 0$ m a^{-1} in the base case, i.e., locations of marine ice accretion. (b) The w_b for the $-1.9°C$ case averaged as in Figure 8a.
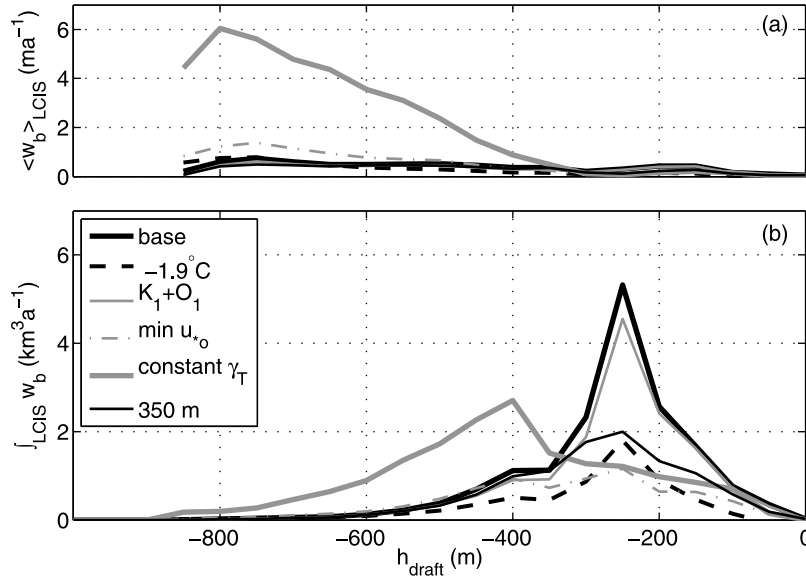
Figure 9. (a) LCIS-averaged w_b over h_{draft} range of -1000 to -50 m in bin intervals of 50 m. (b) LCIS-area-integrated w_b using the same bin intervals as in Figure 9a. The area used for averaging is shown by the dashed box in Figure 2a.

γ_T case show a broader distribution with respect to h_{draft}, and with a maximum contribution from deeper ice than for the base tide-forced case (Figure 9b). Despite the differences in melt rate dependence on h_{draft}, the base and constant γ_T cases have similar total ice volume loss rates of 18.6 km^3 a^{-1} and 19.2 km^3 a^{-1}, respectively (based on the values shown in Figure 9). The similarity of these values is coincidental since we used a value of γ_T taken from the literature rather than one tuned to match the integrated basal melt rate in the base case.

4.6. Comparison of LCIS-Averaged Basal Melt Rates

[62] The basal melt rate averaged over LCIS for our base case is $\langle w_b \rangle_{\mathrm{LCIS}} = 0.21$ m a^{-1} after 10 years of model run time (from results shown in Figure 5a). The corresponding total ice volume loss of 13 km^3 a^{-1} is close to the loss of $\sim$16 km^3 a^{-1} for the "cool case" reported by *Holland et al.* [2009] (who assumed an ocean temperature of -1.9°C). We expect our base case estimate to underpredict the actual basal melt that would occur at -1.7°C because our tidal amplitudes are $\sim$20% lower than those observed by the three GPS locations described in section 3.2.3 and Table 4. The lowest value in our set of simulations compared in Figure 10 was $\sim$0.1 m a^{-1} for our cold case with $\theta_0 = -1.9^\circ$C.

[63] We performed three runs with open ocean tidal forcing scaled by 0.5, 0.75, and 2.0 to incorporate a likely range of uncertainty in tidal currents due to errors in the *wct* grid. The case with tidal currents two times larger than the base case gives the largest value of $\langle w_b \rangle_{\mathrm{LCIS}}$ (0.44 m a^{-1} after $\sim$1 year of model run time). This case roughly approximates the response to a uniform reduction in *wct* of $\sim$50% or generation of more energetic DTVWs than appear in our models; however, the magnitude of this reduction in averaged *wct* is not supported by the comparison with tidal analyses of GPS time series (see section 3.2.3). In general, Figure 10 demonstrates that the ice shelf-averaged basal melt

rates increase nearly linearly in response to increased tide amplification. These results suggest an uncertainty in $\langle w_b \rangle_{\mathrm{LCIS}}$ of 0.15 m a^{-1} given a twofold uncertainty in LCIS-averaged *wct*. In reality, the actual sensitivity will vary depending on the degree and strength of tide-topography interactions.

[64] The min u_{*o} case, which most closely compares to the *Holland et al.* [2009] plume model, shows $\langle w_b \rangle_{\mathrm{LCIS}} = 0.14$ m a^{-1} for $\theta_0 = -1.7^\circ$C, about half that of the base case. The constant γ_T model provides a similar LCIS-averaged w_b and total ice volume loss as the base case, even though the spatial distributions of w_b are very different (Figure 9). The value of $\langle w_b \rangle_{\mathrm{LCIS}}$ for the 350 m case is most similar to the $M_2 + S_2$ case, $\sim$0.19 m a^{-1}. For the range of sensitivity cases described in Table 3, $\langle w_b \rangle_{\mathrm{LCIS}}$ is $\sim$0.11–0.44 m a^{-1} after $\sim$1 year of model run time.

4.7. Cross Front Exchange and Ventilation

[65] We illustrate water mass exchange across the ice shelf front by dye tracers and Lagrangian floats in the 180 day runs initialized from the end of the 10 year base and 350 m cases. Both cases show outflow in the surface level of the northern LCIS (Figures 11a and 11b) and inflow near the seabed along the southern ice front of LCIS (Figures 11c and 11d). The inflow extends $\sim$100 km into the cavity after 180 days, reaching the tip of Kenyon Peninsula. The core of the meltwater plume circulates northeastward across the middle of LCIS (Figure 5b) toward the region of strong recirculation in the NE LCIS. This flow pattern through the center of the cavity differs from that shown by the plume model of *Holland et al.* [2009]. These differences may be attributed to the influence of tide forcing, differences in modeled h_{draft}, and the effect of finite *wct* on the depth-averaged mean circulation.

[66] The 350 m case results show more across-front exchange along the central LCIS, at all depths, than the
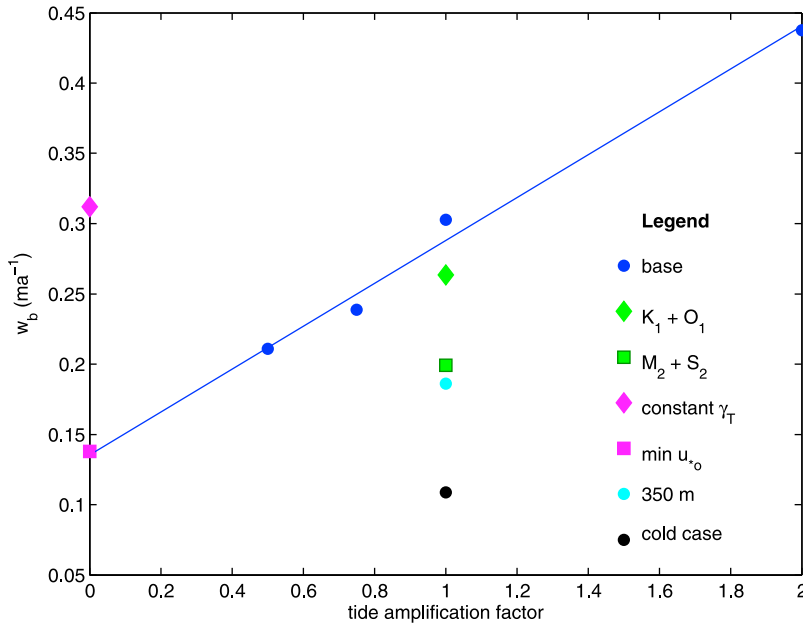
Figure 10. LCIS-averaged values for w_b from the same time interval (model run time 345–375 days) shown in Figure 7. See Table 3 for details of each of these runs. Blue dots are for the base setup, varying the amplification of the tide heights and currents at the forced open boundaries by tide amplification factors of 0.5, 0.75, 1 ("base case"), and 2. The blue line represents a linear least squares fit through the various degrees of tide amplification.

base case (compare Figures 11a and 11b with Figures 11c and 11d). The time series of total dye volume under LCIS shows that, despite these differences in spatial distribution of dye, there is no significant change in the time-averaged net dye volume flux across the LCIS ice front; the cross front exchange for both cases is $\sim 0.2 \times 10^6$ m^{3}s^{-1} (0.2 Sv). Based on this flux across the ice front and our estimate of total ocean volume under the ice shelf, a "ventilation" time scale for LCIS is of order 2–3 years.

[67] Although the net cross-front exchange is equivalent between the base and 350 m cases, the surface level dye export is much stronger in the north for the base case than for the 350 m case. We calculated the volume weighted mean dye concentration for the surface level in the region defined by the white box in Figure 11a and found that the mean concentration of dye (meltwater) in the base case is 1.7 times the concentration of dye within the same region for the 350 m case. We hypothesize that the stronger vorticity gradient across the ice shelf front in the base case is more effective at steering the meltwater outflow to the north where it is eventually forced by the Jason Peninsula to exit the cavity (see also Figure 5b).

[68] Our LCIS results can be compared with a study of the flow regime along Ronne Ice Shelf front [*Makinson*, 2002] where currents along the ice front, even below the depth of the ice base near the front, are strongly steered along the front until summer stratification overcomes the vorticity constraint on deep, across-front exchange. Our results indicate that uncertainties in bathymetry influence across-front exchange. However, factors that are not represented in this study (e.g., wind forcing and stratification) would also influence across-front exchange processes, including providing a seasonal and longer term variability in sub-ice-shelf
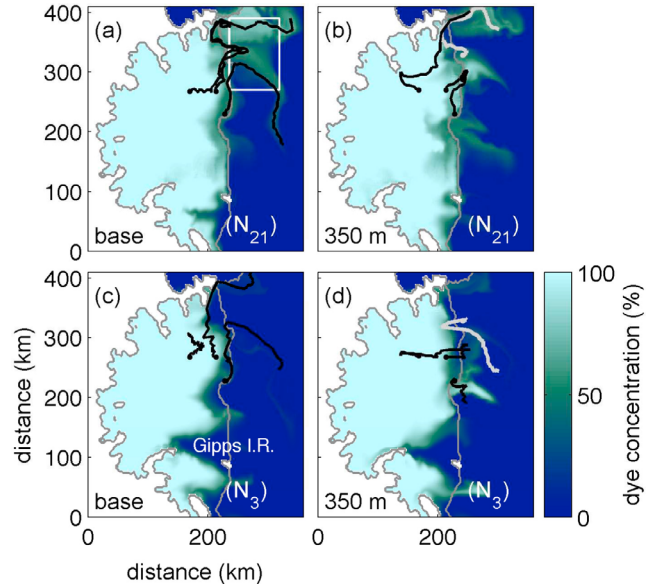

Figure 11. Dye concentration 180 days after being "released" at model run time of 10 years with 100% concentration beneath LCIS and 0% concentration elsewhere. (a, b) Results for the surface (N_{21}) σ level from the base case and 350 m case, respectively. (c, d) Results for the near-bottom (N_3) σ level from the base case and 350 m case, respectively. The black lines are float trajectories that were initialized at the same time as the dye release. These floats were initialized at the surface level at locations [x, y] = [168, 270], [214, 270], and [228, 230] km; they followed the Lagrangian flow path after release. The thick lined gray floats in Figures 11b and 11d were initialized just in front of the ice shelf at [x, y] = [248, 328] km.

ventilation that is not represented in the model results presented here.

4.8. Evaluating the Accuracy of our w_b Predictions

[69] There are only a few direct observations of LCIS w_b, and these are short-term point measurements (N. Gourmelen, personal communication, 2010). The paucity of direct measurements of w_b, simplified model forcing (tides only), and uncertainties in both model geometry and hydrography mean that we cannot unambiguously determine which of our models best represents the real distribution of LCIS basal melt rate. However, we note that the high basal melt rate in the NE region of 2 m a^{-1} in the base case (Figure 5a) is much larger than surface mass balance of <0.5 m a^{-1} (water equivalent) in this region [van de Berg et al., 2006]. Therefore, if this amount of basal melting was occurring, the ice shelf would be thinning rapidly downstream along flow lines, contrary to the observed ice draft map (Figure 2a). In the cold case, maximum melt rate in the NE region is ~0.6 m a^{-1} (Figure 8b), close to surface mass balance and, therefore, more consistent with ice shelf topography. Furthermore, the extent of regions where marine ice accretion is known to occur [Holland et al., 2009] are better represented by the cold case with $\theta_0 = -1.9°C$ than the base case with $\theta_0 = -1.7°C$ (Figure 8).

[70] We propose, therefore, that the cold case is closer to the optimum model for LCIS basal melt than the base case. This is consistent with the conclusion by Nicholls et al. [2004], that LCIS meltwater is produced at the ice-ocean interface with ambient ocean temperatures close to the surface freezing point of ~−1.9°C. The cold case predicts negligible overall melting, $\langle w_b \rangle_{LCIS} \approx 0.1$ m a^{-1} (Figure 10), supporting the view that measured LCIS elevation loss over the last two decades [Zwally et al., 2005; Fricker and Padman, 2012] is due primarily to surface firn compaction including melting [Holland et al., 2011] rather than changes in basal melt rates [Shepherd et al., 2003]. However, we emphasize that the addition of realistic forcing and stratification in the open ocean adjacent to LCIS may significantly change the pattern of melt rate and net mass loss through melting, even if the true inflow temperature is close to −1.9°C.

4.9. Broader Implications

[71] The thickness distribution of an ice shelf is the outcome of a complex mass balance involving the contribution of ice from the grounded ice sheet, lateral divergence of ice mass, surface accumulation (snowfall), basal melting, and iceberg calving. These processes interact with each other through the ice shelf force balance so that changes in the distribution of basal melting will affect inflow, divergence, and calving. Basal melt rate can, in theory, be solved as the residual of the other mass balance terms using ice velocities derived from InSAR and column-integrated ice mass (M) inferred from altimeter-derived surface elevation and density models [e.g., Joughin and Padman, 2003]. In practice, however, it is difficult to create accurate maps of M, especially for ice shelves such as LCIS where column-averaged ice density can change over short distances in response to variations in density and layer thickness of firn [Holland et al., 2009, 2011] and marine ice [Craven et al., 2009].

Uncertainty in M affects ice mass divergence estimates, and further errors arise through a poor understanding of surface accumulation rates. Sensitivity studies, such as those presented here, can help determine the key new measurements required to assess the future stability of LCIS and other ice shelves.

[72] Without tides, melt is concentrated along the deep grounding lines of tributary glaciers (Figure 7e), similar to the pattern reported by Holland et al. [2009]. When tides are included, the extra melt occurs in the NE region (Figure 8); strong diurnal currents in this region of small wct lead to vigorous mixing of ocean heat to the ice base. This increased advection and mixing due to tides, if combined with warming ocean temperatures, could lead to an accelerated thinning in this region with increased likelihood of mass loss through calving [Alley et al., 2008]. However, uncertainty in the map of wct leads to a wide range of plausible distributions of w_b (compare Figures 7a and 7b). When the uncertainty in temperature of the inflowing ocean is also considered, the range of plausible mean basal melt rates (Figure 10) and spatial distributions (Figure 7) is very large.

[73] The sensitivity of tidal current speeds to the distribution of wct indicates that tides can act as a feedback to basal melt rates. The sign of the feedback is not obvious a priori, which complicates the incorporation of basal melt into ice sheet models that attempt to provide long time integrations of ice mass changes [Pollard and DeConto, 2009; Joughin et al., 2010]. We suggest that the change in tidal currents with respect to wct variability should be a focus of future research on LCIS and other ice shelves where tidal currents could be sensitive to fairly small changes in wct.

[74] The three ice shelves for which the importance of tides is now verified through modeling (FRIS [Makinson et al., 2011]; Amery Ice Shelf [Galton-Fenzi, 2009]; and LCIS (this study)) share the characteristics that tidal currents are large compared with innate plume velocities, and the temperature of the inflowing water is close to T_f. We refer to these as "cold water" ice shelves. Preliminary modeling of the Ross Ice Shelf indicate that tides also affect the distribution of basal melting there (S. Springer, personal communication, 2011). The dominance of melt near Ross Ice Shelf front [Horgan et al., 2011] suggests that tides may be particularly effective at increasing near-front basal melting in summer when warm near-surface water can be advected periodically under the ice shelf.

[75] For "warm water" ice shelves with inflow temperatures a few degrees above T_f, such as those fringing the Amundsen Sea, the tidal contribution to w_b may be small because the velocity of the innate thermohaline flows (and, therefore, u_{*o}) is already large [e.g., Payne et al., 2007]. However, several tidal processes might invalidate this assumption. First, as we found for LCIS, tidal rectification can affect the mean advection pathways for ventilation of specific regions of an ice shelf. Second, generation of baroclinic tides by barotropic flow across rough and/or steep topography (at the seabed and at the ice base) may create energetic mixing, both at the ice-ocean boundary and at the interface between a freshwater plume and the underlying ocean. Third, tidal influences near the grounding line are hard to predict because of the generally poor representation

of geometry there. Fourth, it is plausible that tidal interactions with large amplitude, small-scale features in ice base topography (e.g., the quasi-annual "ripples" on Pine Island Ice Shelf [*Bindschadler et al.*, 2011] and the narrow, along-flowline channels on the base of Amery Ice Shelf [*Fricker et al.*, 2009] and Petermann Ice Shelf in NW Greenland [*Rignot and Steffen*, 2008]) may lead to much greater tidal effects than would be predicted from the larger, model-resolved scales of topographic variability. Given these uncertainties, modeling of w_b for any specific ice shelf should include tests with and without tidal forcing rather than excluding tides solely on the basis of weak currents in barotropic tide models.

[76] The sensitivity of w_b to the strength of DTVWs implies that high-resolution grids of *wct* will be required to reduce uncertainties in w_b. Errors in h_{draft} due to uncertainty in the ice density profile may be sufficient to affect modeled tidal currents. This error (up to $\sim$50 m) is comparable to the inferred *wct* in the NE region of LCIS, which means that errors in h_{draft} could result in a large fractional change in *wct*. In addition, the paucity of seabed depth data for most ice shelves implies that even larger errors in *wct* may arise from errors in bathymetry. This is true even for ice shelves whose cavities have been coarsely surveyed by in situ grids of seismic reflectivity (e.g., FRIS [*Johnson and Smith*, 1997] and Ross Ice Shelf [*Greischar and Bentley*, 1980]), since typical seismic station spacing (50–100 km) is much greater than the topographic length scales associated with DTVWs.

[77] A conservative requirement for grid spacing is the ability to resolve the internal Rossby radius of deformation, which is $\sim$5 km at polar latitudes; this requirement implies an ideal model grid spacing of $\sim$1–2 km. While the ice shelf surface can be mapped at this resolution by aircraft altimeters, the prospects for high-resolution mapping of *D* are, presently, poor.

5. Conclusions

[78] We applied the Regional Ocean Modeling System (version 3.2) with thermodynamic coupling between a nonevolving ice shelf and the ocean to quantify the sensitivity of LCIS basal melt rate (w_b) to tidal forcing, water column thickness (*wct*) distribution, initial ocean potential temperature (θ_0) and parameterizations of ice-ocean thermodynamic exchange. From our study, we reach the following LCIS-specific conclusions.

[79] 1. For the range of simulations reported here, ice shelf-averaged basal melt rate $\langle w_b \rangle_{\mathrm{LCIS}}$ is $\sim$0.11–0.44 m a^{-1}, corresponding to 7–27 km^3 a^{-1} (6–24 Gt a^{-1}) total ice loss. For most of our simulations, net mass loss primarily occurs where ice draft is between 100 and 350 m. The locations of regions of high melt rates vary from one simulation to another.

[80] 2. In a model run without tidal forcing, regions of relatively rapid melt are found near the deep grounding lines of glaciers feeding LCIS. Melt rates elsewhere are negligible. When tides are added, w_b increases in the NE region of LCIS, and along the edges of the Churchill and Kenyon peninsulas.

[81] 3. For $\theta_0 = -1.7°C$, adding tidal forcing approximately doubles $\langle w_b \rangle_{\mathrm{LCIS}}$ relative to a model forced only by thermohaline exchanges between the ocean and ice base. The tide-induced increase in $\langle w_b \rangle_{\mathrm{LCIS}}$ is due primarily to

significant enhancement of w_b in the NE region of LCIS; in this region, diurnal topographic vorticity waves (DTVWs) excited by tidal interactions with gradients in *wct* create strong tidal currents (up to $\sim$0.4 m s^{-1}) with the consequence of increased basal melting. However, accurate prediction of tidal currents in this region is difficult. Our model domain omits Bawden Ice Rise, whose presence suggests that there may be significant regions where *wct* is less than our imposed minimum value of 100 m, and the real flux of tidal energy as DTVWs along the ice front and into the cavity will be different than in our model. The errors in sub-ice-shelf geometry (including the omission of Bawden Ice Rise and model limitations on resolving DTVWs) imply a factor of $\sim$2 uncertainty in $\langle w_b \rangle_{\mathrm{LCIS}}$.

[82] 4. With the base case geometry, tides generate a rectified barotropic circulation whose magnitude (up to $\sim$0.05 m s^{-1} in regions of strong tidal currents) can exceed typical thermohaline flows. The rectified tidal flow may, therefore, contribute to the ventilation of the sub-ice-shelf cavity and the fate of freshwater as it circulates under LCIS.

[83] 5. The sensitivity of w_b and tide-induced mean circulation to the energetics of DTVWs implies that high-resolution grids of ice draft and seabed bathymetry will be required to minimize uncertainties in w_b. Studies of DTVWs along the continental slope [*Middleton et al.*, 1987; *Padman et al.*, 1992] demonstrate that cross-slope length scales of these waves are similar to the cross-slope scale of topographic variability. These scales can be very small close to the ice front, with large fractional changes in *wct* over a distance of order 1 km. Under the bulk of the ice shelf, large channels with scales of order 1–10 km are found; however, their contribution to DTVWs is uncertain. A conservative estimate of required grid resolution is the ability to resolve the baroclinic Rossby radius of deformation, $\sim$5 km in high-latitude seas, implying a model grid spacing of $\delta x \sim$1 km.

[84] 6. With forcing only from tides and ice-ocean thermohaline exchange, the volume flux across the ice front is $\sim$0.2 Sv, corresponding to a mean ventilation time of 2–3 years for the LCIS cavity.

[85] 7. For the cold case with $\theta_0 = -1.9°C$, $\langle w_b \rangle_{\mathrm{LCIS}}$ is reduced by a factor of $\sim$3 relative to our base case with $\theta_0 = -1.7°C$.

[86] 8. A commonly used model with constant γ_T, corresponding to a total current speed that is constant under the entire ice shelf, predicts high melt rates in the grounding zone but relatively low melt rates elsewhere. The sensitivity of this parameterization to pressure guarantees maximum melt rates at the grounding line for conditions of uniform temperature; as such, this parameterization may produce distributions of ice shelf basal melt that are inconsistent with the real spatial pattern, yielding mass and force balances that are biased accordingly.

[87] 9. From comparisons with available data, we tentatively conclude that our cold case ($\theta_0 = -1.9°C$) is our best representation of LCIS basal melting under current oceanographic conditions. This case provides: estimates of w_b in the NE region that are consistent with observed changes in ice shelf geometry, predictions of marine ice accumulation regions that are more consistent with the marine ice accumulation zones shown by *Holland et al.* [2009], and agreement with the inflow temperature inferred by *Nicholls et al.* [2004]. However, since our model lacks realistic ocean

stratification, atmospheric forcing and sea ice effects, the true pattern and magnitude of w_b may be different from our cold case simulation.

[88] We conclude that the accuracy of w_b predictions is undermined by potential errors in sub-ice-shelf geometry and ocean hydrography such that there is an urgent need for new data sets to adequately constrain models of ice shelf and ocean interactions. The most promising approaches to large-scale mapping of ice shelf geometry come from airborne altimetry and gravity surveys over ice shelves [*Cochran and Bell*, 2012]. However, improved data sets for conversion of ice surface height to ice draft are also required, either through remote sensing methods [*Holland et al.*, 2011] or in situ density measurements [*Jansen et al.*, 2010]. Hydrographic data are needed for all seasons in order to determine the temperature of inflow and its seasonal variability. Given the strong spatial variability of cross-front exchange suggested by our dye experiments (Figure 11), data must be collected at several locations along the entire length of an ice front. For FRIS and LCIS, this remains a significant challenge because of the thick, year-round sea ice cover typical of the southern and western Weddell Sea. Until these improved data sets become available, numerical studies of ice shelf basal melt should cite basal melt rates in the context of potential errors from modeling uncertainties in geometry, hydrography and atmospheric forcing.

References

Alley, R. B., H. J. Horgan, I. Joughin, K. M. Cuffey, T. K. Dupont, B. R. Parizek, S. Anandakrishnan, and J. Bassis (2008), A simple law for ice-shelf calving, *Science*, 322, 1344–1344, doi:10.1126/science.1162543.

Bathmann, U., V. Smetacek, H. de Baar, E. Fahrbach, and G. Krause (1994), The expeditions ANTARKTIS X/6-8 of the research vessel "POLARSTERN" in 1992/1993, technical report, Alfred-Wegener-Inst. for Polar and Mar. Res., Bremerhaven, Germany.

Beckmann, A., H. H. Hellmer, and R. Timmermann (1999), A numerical model of the Weddell Sea: Large-scale circulation and water mass distribution, *J. Geophys. Res.*, 104(C10), 23,375–23,391.

Bindschadler, R., D. G. Vaughan, and P. Vornberger (2011), Variability of basal melt beneath the Pine Island Glacier Ice Shelf, West Antarctica, *J. Glaciol.*, 57(204), 581–595.

Cartwright, D. E. (1969), Extraordinary tidal currents near St. Kilda, *Nature*, 223, 928–930.

Chapman, D. (1985), Numerical treatment of cross-shelf open boundaries in a barotropic coastal ocean model, *J. Phys. Oceanogr.*, 19, 384–391.

Cochran, J., and R. Bell (2012), Inversion of IceBridge gravity data for continental shelf bathymetry beneath the Larsen Ice Shelf, *J. Glaciol.*, in press.

Comiso, J. (2000), Variability and trends in Antarctic surface temperatures from in situ and satellite infrared measurements, *J. Clim.*, 13, 1674–1696.

Cook, A. J., and D. G. Vaughan (2010), Overview of areal changes of the ice shelves on the Antarctic Peninsula over the past 50 years, *Cryosphere*, 4, 77–98.

Craven, M., I. Allison, H. Fricker, and R. Warner (2009), Properties of a marine ice layer under the Amery Ice Shelf, East Antarctica, *J. Glaciol.*, 55(192), 717–728.

Dinniman, M. S., J. M. Klinck, and W. O. Smith Jr. (2007), Influence of sea ice cover and icebergs on circulation and water mass formation in a numerical circulation model of the Ross Sea, Antarctica, *J. Geophys. Res.*, 112, C11013, doi:10.1029/2006JC004036.

Dinniman, M. S., J. M. Klinck, and W. O. Smith (2011), A model study of Circumpolar Deep Water on the West Antarctic Peninsula and Ross Sea continental selves, *Deep Sea Res., Part II*, 58, 1508–1523, doi:10.1016/j.dsr2.2010.11.013.

Drewry, D., S. Jordan, and E. Jankowski (1982), Measured properties of the Antarctic Ice Sheet: Surface configurations, ice thickness, volume and bedrock characteristics, *Ann. Glaciol.*, 3, 83–91.

Flather, R. (1976), A tidal model of the northwest European continental shelf, *Mem. Soc. R. Sci. Liege*, 6, 141–164.

Foldvik, A., and T. Kvinge (1974), Conditional instability of sea water at the freezing point, *Deep Sea Res. Oceanogr. Abstr.*, 21, 169–174.

Fricker, H. A., and L. Padman (2002), Tides on Filchner-Ronne Ice Shelf from ERS radar altimetry, *Geophys. Res. Lett.*, 29(12), 1622, doi:10.1029/2001GL014175.

Fricker, H. A., and L. Padman (2012), Thirty years of elevation change on Antarctic Peninsula ice shelves from multimission satellite radar altimetry, *J. Geophys. Res.*, 117, C02026, doi:10.1029/2011JC007126.

Fricker, H. A., R. Coleman, L. Padman, T. A. Scambos, J. Bohlander, and K. M. Brunt (2009), Mapping the grounding zone of the Amery Ice Shelf, East Antarctica using InSAR, MODIS and ICESat, *Antarct. Sci.*, 21(5), 515–532, i10.1017/S095410200999023X.

Gade, H. G. (1979), Melting of ice in sea water: A primitive model with application to the Antarctic Ice Shelf and icebergs, *J. Phys. Oceanogr.*, 9(1), 189–198.

Galton-Fenzi, B. K. (2009), Modelling ice-shelf/ocean interaction, PhD dissertation, Quant. Mar. Sci., Commonw. Sci. and Ind. Re. Organ., Univ. of Tasmania, Hobart, Australia.

Galton-Fenzi, B. K., C. Maraldi, R. Coleman, and J. Hunter (2008), The cavity under the Amery Ice Shelf, East Antarctica, *J. Glaciol.*, 54(188), 881–887.

Gill, A. E., and E. H. Schumann (1974), The generation of long shelf waves by the wind, *J. Phys. Oceanogr.*, 4(1), 83–90.

Greischar, L., and C. Bentley (1980), Isostatic equilibrium grounding line between the West Antarctic inland ice sheet and the Ross Ice Shelf, *Nature*, 283, 641–654, doi:10.1038/283651a0.

Grosfeld, K., R. Gerdes, and J. Determann (1997), Thermohaline circulation and interaction between ice shelf cavities and the adjacent open ocean, *J. Geophys. Res.*, 102(C7), 15,595–15,610.

Hall, J. (2006), GEBCO Centennial Special Issue—Charting the secret world of the ocean floor: the GEBCO project 1903–2003, *Mar. Geophys. Res.*, 27, 1–5, doi:10.1007/s11001-006-8181-4.

Haney, R. L. (1991), On the pressure-gradient force over steep topography in sigma coordinate ocean models, *J. Phys. Oceanogr.*, 21(4), 610–619.

Hellmer, H. H., and D. J. Olbers (1989), A two-dimensional model for the thermohaline circulation under an ice shelf, *Antarct. Sci.*, 1(4), 325–336.

Holland, D. M., and A. Jenkins (1999), Modeling thermodynamic ice-ocean interactions at the base of an ice shelf, *J. Phys. Oceanogr.*, 29(8), 1787–1800.

Holland, P. R. (2008), A model of tidally dominated ocean processes near ice shelf grounding lines, *J. Geophys. Res.*, 113, C11002, doi:10.1029/2007JC004576.

Holland, P. R., and D. L. Feltham (2006), The effect of rotation and ice shelf topography on frazil-laden ice shelf water plumes, *J. Phys. Oceanogr.*, 36(12), 2312–2327, doi:10.1175/JPO2970.1.

Holland, P. R., D. L. Feltham, and A. Jenkins (2007), Ice Shelf Water plume flow beneath Filchner-Ronne Ice Shelf, Antarctica, *J. Geophys. Res.*, 112, C05044, doi:10.1029/2006JC003915.

Holland, P. R., H. F. J. Corr, D. G. Vaughan, and A. Jenkins (2009), Marine ice in Larsen Ice Shelf, *Geophys. Res. Lett.*, 36, L11604, doi:10.1029/2009GL038162.

Holland, P. R., H. F. J. Corr, H. D. Pritchard, D. G. Vaughan, R. J. Arthern, A. Jenkins, and M. Tedesco (2011), The air content of Larsen Ice Shelf, *Geophys. Res. Lett.*, 38, L10503, doi:10.1029/2011GL047245.

Horgan, H. J., R. T. Walker, S. Anandakrishnan, and A. R. B. (2011), Surface elevation changes at the front of the Ross Ice Shelf: Implications for basal melting, *J. Geophys. Res.*, 116, C02005, doi:10.1029/2010JC006192.

Hunkins, K. (1986), Anomalous diurnal tidal currents on the Yarmak Plateau, *J. Mar. Res.*, 44, 51–69.

Jacobs, S. S. (2004), Bottom water production and its links with the thermohaline circulation, *Antarct. Sci.*, 16(4), 427–437, doi:10.1017/S095410200400224X.

Jacobs, S. S., H. H. Helmer, C. S. M. Doake, A. Jenkins, and R. M. Frolich (1992), Melting of ice shelves and the mass balance of Antarctica, *J. Glaciol.*, 38(130), 375–387.

Jansen, D., B. Kulessa, P. Sammonds, A. Luckman, E. King, and N. Glasser (2010), Present stability of the Larsen C Ice Shelf, Antarctic Peninsula, *J. Glaciol.*, 56(198), 593–600.

Jarvis, E., and E. King (1993), The seismic wavefield recorded on an Antarctic ice shelf, *J. Seismol. Explor.*, 2, 69–86.

Jenkins, A. (2011), Convection-driven melting near the grounding lines of ice shelves and tidewater glaciers, *J. Phys. Oceanogr.*, 41, 2279–2294, doi:10.1175/JPO-D-11-03.1.

Jenkins, A., H. H. Hellmer, and D. M. Holland (2001), The role of meltwater advection in the formulation of conservative boundary conditions at an ice-ocean interface, *J. Phys. Oceanogr.*, 31(1), 285–296.

Jenkins, A., K. W. Nicholls, and H. F. J. Corr (2010), Observations and parameterization of ablation at the base of Ronne Ice Shelf, Antarctica, *J. Phys. Oceanogr.*, 40, 2298–2312.

Johnson, M. R., and A. M. Smith (1997), Seabed topography under the southern and western Ronne Ice Shelf, derived from seismic surveys, *Antarct. Sci.*, 9(2), 201–208.

Joughin, I., and L. Padman (2003), Melting and freezing beneath Filchner-Ronne Ice Shelf, Antarctica, *Geophys. Res. Lett.*, 30(9), 1477, doi:10.1029/2003GL016941.

Joughin, I., B. E. Smith, I. M. Howat, T. Scambos, and T. Moon (2010), Greenland flow variability from ice-sheet-wide velocity mapping, *J. Glaciol.*, 56(197), 415–430.

Khazendar, A., E. Rignot, and E. Larour (2011), Acceleration and spatial rheology of Larsen C Ice Shelf, Antarctic Peninsula, *Geophys. Res. Lett.*, 38, L09502, doi:10.1029/2011GL046775.

King, M. A., L. Padman, K. Nicholls, P. J. Clarke, G. H. Gudmundsson, B. Kulessa, and A. Shepherd (2011), Ocean tides in the Weddell Sea: New observations on the Filchner-Ronne and Larsen C ice shelves and model validation, *J. Geophys. Res.*, 116, C06006, doi:10.1029/2011JC006949. (Correction to "Ocean tides in the Weddell Sea: New observations on the Filchner-Ronne and Larsen C ice shelves and model validation," *J. Geophys. Res.*, 116, C08026, doi:10.1029/2011JC007463.)

Lewis, E. L., and R. G. Perkin (1986), Ice pumps and their rates, *J. Geophys. Res.*, 91(C10), 11,756–11,762.

Little, C. M., A. Gnanadesikan, and R. Hallberg (2008), Large-scale oceanographic constraints on the distribution of melting and freezing under ice shelves, *J. Phys. Oceanogr.*, 38(10), 2242–2255.

Little, C. M., A. Gnanadesikan, and M. Oppenheimer (2009), How ice shelf morphology controls basal melting, *J. Geophys. Res.*, 114, C12007, doi:10.1029/2008JC005197.

Little, C. M., D. Goldberg, A. Gnanadesikan, and M. Oppenheimer (2012), On the coupled response to ice shelf basal melting, *J. Glaciol.*, 58(208), 203–215, doi:10.3189/2012JoG11J037

Loder, J. (1980), Topographic Rectification of tidal currents on the sides of Georges Bank, *J. Phys. Oceanogr.*, 10(9), 1399–1416.

Losch, M. (2008), Modeling ice shelf cavities in a z-coordinate ocean general circulation model, *J. Geophys. Res.*, 113, C08043, doi:10.1029/2007JC004368.

Luckman, A., L. Padman, and D. Jansen (2010), Persistent iceberg groundings in the western Weddell Sea, Antarctica, *Remote Sens. Environ.*, 114(2), 385–391, doi:10.1016/j.rse.2009.09.009.

Lythe, M. B., D. G. Vaughan, and the BEDMAP Consortium (2001), BEDMAP: A new ice thickness and subglacial topographic model of Antarctica, *J. Geophys. Res.*, 106, 11,335–11,351.

MacAyeal, D. R. (1984), Thermohaline circulation below the Ross Ice Shelf: A consequence of tidally induced vertical mixing and basal melting, *J. Geophys. Res.*, 89(C1), 597–606.

MacAyeal, D. R. (1985a), Tidal rectification below the Ross Ice Shelf, Antarctica, in *Oceanology of the Antarctic Continental Shelves*, *Antarct. Res. Ser.*, vol. 43, edited by S. Jacobs, pp. 133–144, AGU, Washington, D. C.

MacAyeal, D. R. (1985b), Evolution of tidally triggered meltwater plumes below ice shelves, in *Oceanology of the Antarctic Continental Shelves*, *Antarct. Res. Ser.*, vol. 43, edited by S. Jacobs, pp. 109–132, AGU, Washington, D. C.

Mackensen, A. (2001), Oxygen and carbon stable isotope tracers of Weddell Sea water masses: New data and some paleoceanographic implications, *Deep Sea Res., Part I*, 48(6), 1401–1422, doi:10.1016/S0967-0637(00)00093-5.

Makinson, K. (2002), Modeling tidal current profiles and vertical mixing beneath Filchner-Ronne Ice Shelf, Antarctica, *J. Phys. Oceanogr.*, 32(1), 202–215.

Makinson, K., and K. Nicholls (1999), Modeling Tidal currents beneath Filchner-Ronne Ice Shelf and on the adjacent continental shelf: Their effect on mixing and transport, *J. Geophys. Res.*, 104(C6), 13,449–13,465.

Makinson, K., M. Schroder, and S. Osterhus (2006), Effect of critical latitude and seasonal stratification on tidal current profiles along Ronne Ice Front, Antarctica, *J. Geophys. Res.*, 111, C03022, doi:10.1029/2005JC003062.

Makinson, K., P. Holland, A. Jenkins, K. W. Nicholls, and D. M. Holland (2011), Influence of tides on melting and freezing beneath Filchner-Ronne Ice Shelf, Antarctica, *Geophys. Res. Lett.*, 38, L06601, doi:10.1029/2010GL046462.

McPhee, M. G. (2008), *Air-Ice-Ocean Interaction: Turbulent Ocean Boundary Layer Exchange Processes*, Springer, Berlin.

McPhee, M. G., J. H. Morison, and F. Nilsen (2008), Revisiting heat and salt exchange at the ice-ocean interface: Ocean flux and modeling considerations, *J. Geophys. Res.*, 113, C06014, doi:10.1029/2007JC004383.

Mellor, G., and T. Yamada (1974), A hierarchy of turbulence closure models for planetary boundary layers, *J. Atmos. Sci.*, 13, 1791–1806.

Mellor, G., and T. Yamada (1982), Development of a turbulence closure model for geophysical fluid problems, *Rev. Geophys. Space Phys.*, 20, 851–875.

Middleton, J., T. Foster, and A. Foldvik (1987), Diurnal shelf waves in the southern Weddell Sea, *J. Phys. Oceanogr.*, 17, 784–791.

Motyka, R., L. Hunter, K. Echelmeyer, and C. Connor (2003), Submarine melting at the terminus of a temperate tidewater glacier, LeConte Glacier, Alaska, USA, *Ann. Glaciol.*, 36, 57–65.

Motyka, R., M. Truffer, M. Fahnestock, J. Mortensen, S. Rysgaard, and I. Howat (2011), Submarine melting of the 1985 Jakobshavn Isbræ floating tongue and the triggering of the current retreat, *J. Geophys. Res.*, 116, F01007, doi:10.1029/2009JF001632.

Nicholls, K. W., K. Makinson, and M. R. Johnson (1997), New oceanographic data from beneath Ronne Ice Shelf, Antarctica, *Geophys. Res. Lett.*, 24(2), 167–170.

Nicholls, K. W., C. J. Pudsey, and P. Morris (2004), Summertime water masses off the northern Larsen C Ice Shelf, Antarctica, *Geophys. Res. Lett.*, 31, L09309, doi:10.1029/2004GL019924.

Padman, L., and C. Kottmeier (2000), High-frequency ice motion and divergence in the Weddell Sea, *J. Geophys. Res.*, 105(C2), 3379–3400.

Padman, L., A. J. Plueddemann, R. D. Muench, and R. Pinkel (1992), Diurnal tides near the Yermak Plateau, *J. Geophys. Res.*, 97(C8), 12,639–12,652.

Padman, L., H. A. Fricker, R. Coleman, S. Howard, and S. Erofeeva (2002), A new tidal model for the Antarctic ice shelves and seas, *Ann. Glaciol.*, 34, 247–254.

Padman, L., S. Y. Erofeeva, and H. A. Fricker (2008), Improving Antarctic tide models by assimilation of ICESat laser altimetry over ice shelves, *Geophys. Res. Lett.*, 35, L22504, doi:10.1029/2008GL035592.

Padman, L., S. L. Howard, A. H. Orsi, and R. D. Muench (2009), Tides of the northwestern Ross Sea and their impact on dense outflows of Antarctic Bottom Water, *Deep Sea Res., Part II*, 56(13–14), 818–834, doi:10.1016/j.dsr2.2008.10.026.

Payne, A. J., A. Vieli, A. P. Shepherd, D. J. Wingham, and E. Rignot (2004), Recent dramatic thinning of largest West Antarctic ice stream triggered by oceans, *Geophys. Res. Lett.*, 31, L23401, doi:10.1029/2004GL021284.

Payne, A. J., P. R. Holland, A. P. Shepherd, I. C. Rutt, A. Jenkins, and I. Joughin (2007), Numerical modeling of ocean-ice interactions under Pine Island Bay's ice shelf, *J. Geophys. Res.*, 112, C10019, doi:10.1029/2006JC003733.

Pollard, D., and R. M. DeConto (2009), Modelling West Antarctic ice sheet growth and collapse through the past five million years, *Nature*, 458, 329–332, doi:10.1038/nature07809.

Potter, J., and J. Paren (1985), Interaction between ice shelf and ocean in George VI Sound, Antarctica, *Antarct. Res. Ser.*, 43, 35–58.

Rignot, E., and S. S. Jacobs (2002), Rapid bottom melting widespread near Antarctic ice sheet grounding lines, *Science*, 296, 2020–2023, doi:10.1126/science.1070942.

Rignot, E., and K. Steffen (2008), Channelized bottom melting and stability of floating ice shelves, *Geophys. Res. Lett.*, 35, L02503, doi:10.1029/2007GL031765.

Rignot, E., G. Casassa, P. Gogineni, W. Krabill, A. Rivera, and R. Thomas (2004), Accelerated ice discharge from the Antarctic Peninsula following the collapse of Larsen B Ice Shelf, *Geophys. Res. Lett.*, 31, L18401, doi:10.1029/2004GL020697.

Rignot, E., J. L. Bamber, M. R. Van Den Broeke, C. Davis, Y. H. Li, W. J. Van De Berg, and E. Van Meijgaard (2008), Recent antarctic ice mass loss from radar interferometry and regional climate modelling, *Nat. Geosci.*, 1(2), 106–110.

Rignot, E., M. Koppes, and I. Velicogna (2010), Rapid submarine melting of the calving faces of West Greenland glaciers, *Nat. Geosci.*, 3(3), 187–191, doi:10.1038/NGEO765.

Robertson, R., L. Padman, and G. Egbert (1998), Tides in the Weddell Sea, in *Oceanology of the Antarctic Continental Shelf*, *Antarct. Res. Ser.*, vol. 75, edited by S. Jacobs and R. Weiss, pp. 341–369, AGU, Washington, D. C.

Robertson, R., M. Visbeck, A. L. Gordon, and E. Fahrbach (2001), Internal tides and baroclinicity in the Southern Weddell Sea 2. Effects of the critical latitude and stratification, *J. Geophys. Res.*, *106*(C11), 27,017–27,034.

Robinson, I. (1981), Tidal vorticity and residual circulation, *Deep Sea Res., Part A*, *28*(3), 195–212.

Robinson, N., M. Williams, P. Barrett, and A. Pyne (2010), Observations of flow and ice-ocean interaction beneath the McMurdo Ice Shelf, Antarctica, *J. Geophys. Res.*, *115*, C03025, doi:10.1029/2008JC005255.

Scambos, T., C. Hulbe, and M. Fahnestock (2003), Climate-induced ice shelf disintegration in the Antarctic Peninsula, in *Antarctic Peninsula Climate Variability: Historical and Paleoenvironmental Perspectives*, *Antarct. Res. Ser.*, vol. 79, edited by E. Domack et al., pp. 79–92, AGU, Washington, D. C., doi:10.1029/AR079p0079.

Scambos, T. A., J. A. Bohlander, C. A. Shuman, and P. Skvarca (2004), Glacier acceleration and thinning after ice shelf collapse in the Larsen B embayment, Antarctica, *Geophys. Res. Lett.*, *31*, L18402, doi:10.1029/2004GL020670.

Shchepetkin, A. F., and J. C. McWilliams (2009), Correction and commentary for "Ocean forecasting in terrain-following coordinates: Formulation and skill assessment of the regional ocean modeling system" by Haidvogel et al., J. Comp. Phys. 227, pp. 3595–3624), *J. Compus. Phys.*, *228*(24), 8985–9000, doi:10.1016/j.jcp.2009.09.002.

Shepherd, A., D. Wingham, T. Payne, and P. Skvarca (2003), Larsen Ice Shelf has progressively thinned, *Science*, *302*, 856–859, doi:10.1126/science.1089768.

Sirevaag, A. (2009), Turbulent exchange coefficients for the ice/ocean interface in case of rapid melting, *Geophys. Res. Lett.*, *36*, L04606, doi:10.1029/2008GL036587.

Skvarca, P., W. Rack, H. Rott, and T. I. Y. Donangelo (1998), Evidence of recent climatic warming on the Eastern Antarctic Peninsula, *Ann. Glaciol.*, *27*, 628–632.

Skvarca, P., W. Rack, H. Rott, and T. I. Y. Donangelo (1999), Climatic trend and the retreat and disintegration of ice shelves on the Antarctic Peninsula: An overview, *Polar Res.*, *18*, 151–157.

Smith, W. H. F., and D. T. Sandwell (1997), Global seafloor topography from satellite altimetry and ship depth soundings, *Science*, *277*, 1957–1962, doi:10.1126/science.277.5334.1956.

Thomson, R. E., and W. A. Crawford (1982), The generation of diurnal period shelf waves by tidal currents, *J. Geophys. Res.*, *12*, 635–643.

van de Berg, W., M. van den Broeke, C. Reijmer, and E. van Meijgaard (2006), Reassessment of the Antarctic surface mass balance using calibrated output of a regional atmospheric climate model, *J. Geophys. Res.*, *111*, D11104, doi:10.1029/2005JD006495.

van den Broeke, M., W. J. van de Berg, and E. van Meijgaard (2008), Firn depth correction along the Antarctic grounding line, *Antarct. Sci.*, *20*, 513–517, doi:10.1017/S095410200800148X.

Vaughan, D. G., and C. S. M. Doake (1996), Recent atmospheric warming and retreat of ice shelves on the Antarctic Peninsula, *Nature*, *379*, 328–331.

Vieli, A., A. J. Payne, A. Shepherd, and Z. Du (2007), Causes of pre-collapse changes of the Larsen B ice shelf: Numerical modelling and assimilation of satellite observations, *Earth Planet. Sci. Lett.*, *259*(3–4), 297–306, doi:10.1016/j.epsl.2007.04.050.

Zwally, H., M. Giovinetto, J. Li, H. Cornejo, M. Beckley, A. Brenner, J. Saba, and D. Yi (2005), Mass changes of the Greenland and Antarctic ice sheets and shelves and contributions to sea-level rise: 1992–2002, *J. Glaciol.*, *51*(175), 509–527, doi:10.3189/172756505781829007.

M. S. Dinniman, Center for Coastal Physical Oceanography, Old Dominion University, Innovations Research Bldg. 1, 3rd Floor, 4111 Monarch Way, Norfolk, VA 23508, USA. (msd@ccpo.odu.edu)

S. Y. Erofeeva and R. D. Mueller, College of Earth, Ocean, and Atmospheric Sciences, Oregon State University, 104 COAS Administration Bldg., Corvallis, OR 97331-5503, USA. (serofeev@coas.oregonstate.edu; rmueller@coas.oregonstate.edu)

H. A. Fricker, Institute of Geophysics and Planetary Physics, Scripps Institution of Oceanography, UCSD, 9500 Gilman Dr., La Jolla, CA 92093, USA. (hafricker@ucsd.edu)

M. A. King, School of Civil Engineering and Geosciences, Newcastle University, Cassie Bldg., Newcastle upon Tyne NE1 7RU, UK. (m.a.king@newcastle.ac.uk)

L. Padman, Earth & Space Research, 3350 SW Cascade Ave., Corvallis, OR 97333-1536, USA. (padman@esr.org)